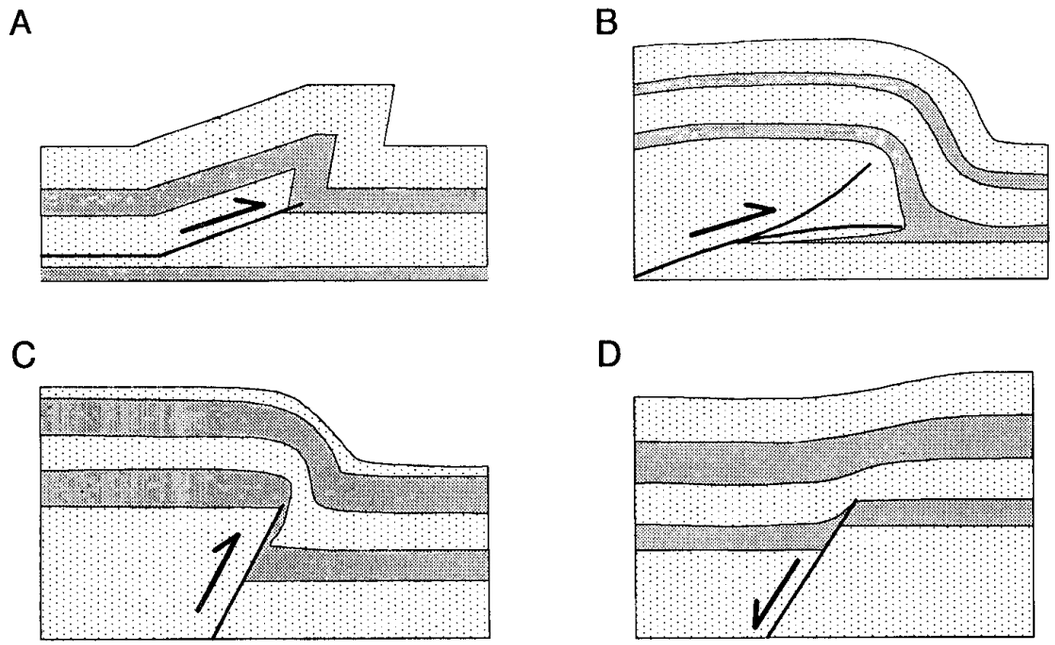

***Figure 1.* Models of fault-propagation folds. A: Geometric kink-band model (Suppe and Medwedeff, 1984). B, C, D: Analog experimental models of folds above thrust (B; Chester et al., 1988), reverse (C; Friedman et al., 1980), and normal (D; Withjack et al., 1990) faults.**

Erslev, 1991

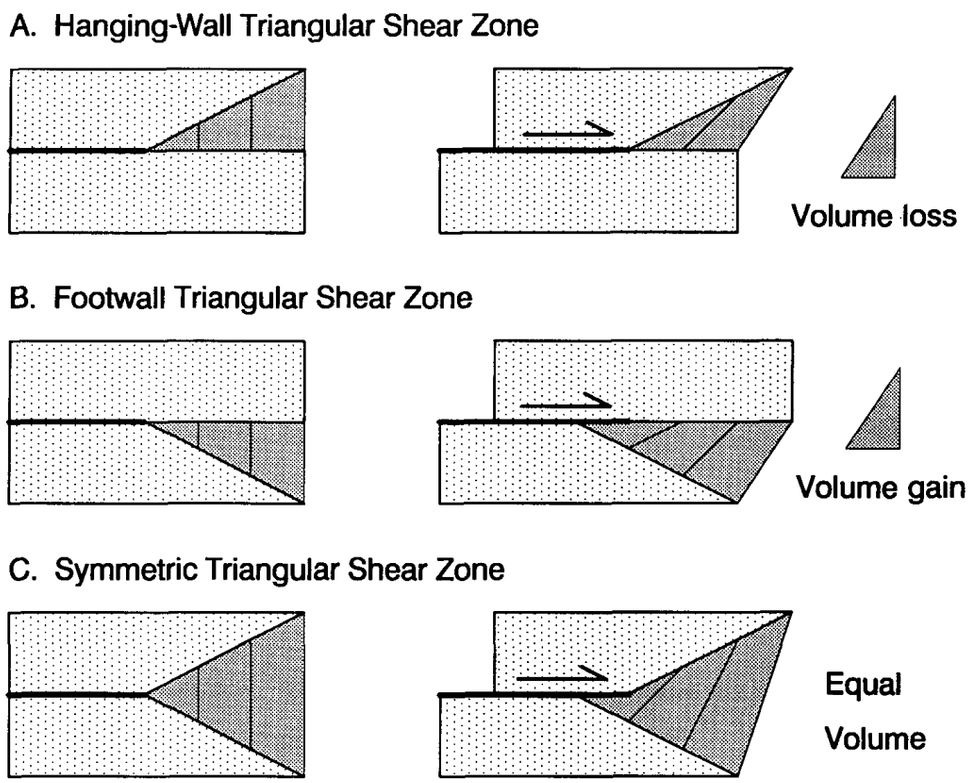

Figure 2. Geometric end members of triangular shear-zone folding.

Erslev, 1991

With the deformation in the trishear, this style of reconstruction conserves area but not necessarily line lengths in the plastically deforming zone.

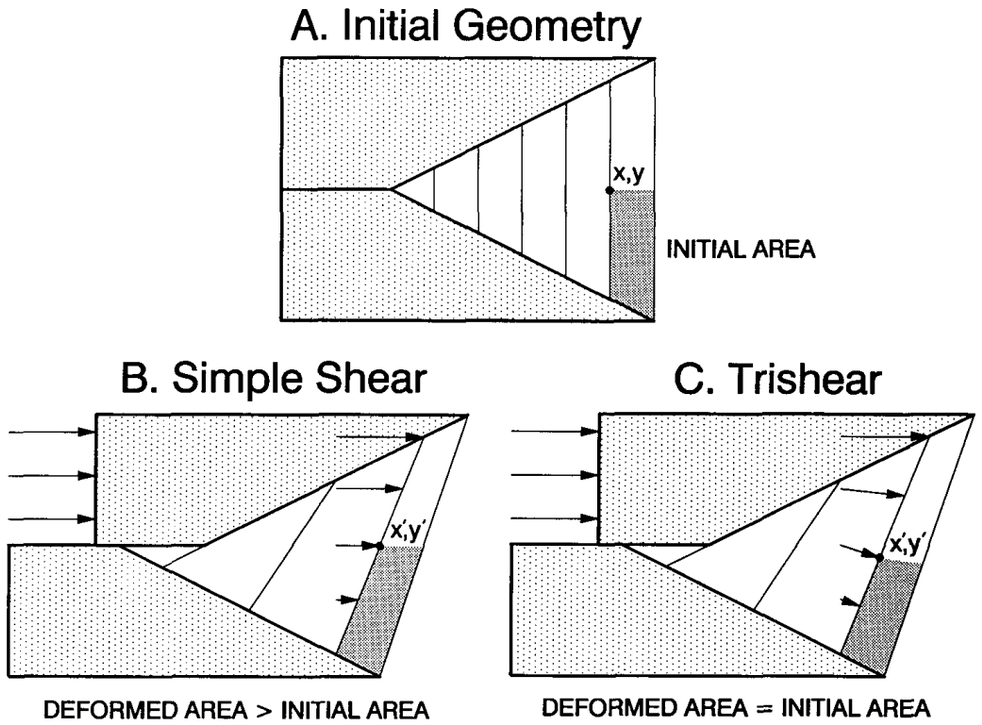

Figure 3. Simple shear and trishear approximations of homogeneous shear in triangular shear zones.

Erslev, 1991

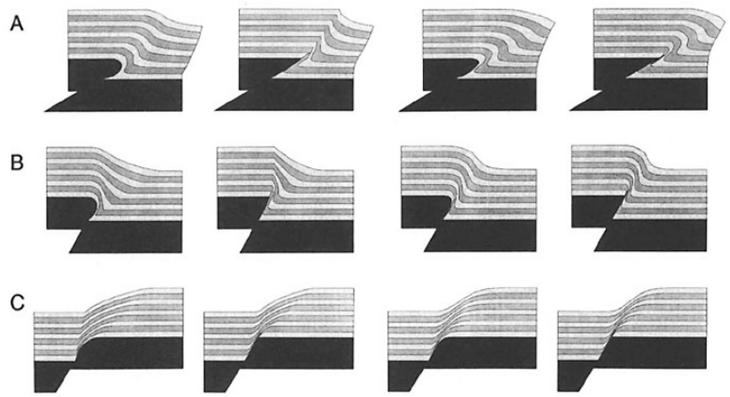

Figure 4. TRISHEAR-generated, homogeneous and heterogeneous fault-propagation folding above (A) thrust (30° dip, 60° apex angle), (B) reverse (60° dip, 60° apex angle), and (C) normal (60° dip, 40° apex angle) faults.

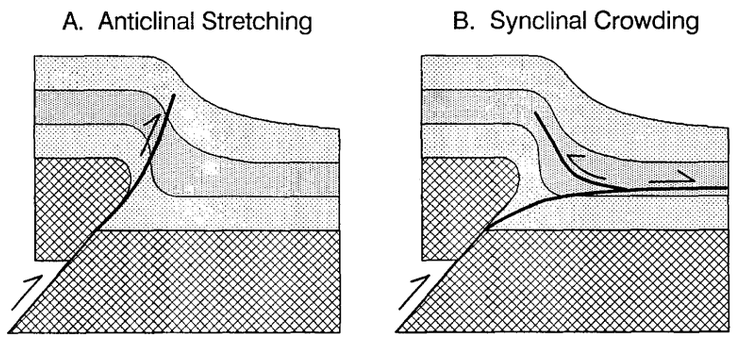

Figure 5. Fault-propagation trajectories suggested by homogeneous, footwall-fixed trishear in front of thrust faults (45° dip, 60°apex angle).

Advantages:

Deals with more realistic geometries in foreland situations than fault-bend folds

Disadvantages:

Requires plastic deformation in trishear zone, which can become non-unique in terms of structures

Erslev, 1991

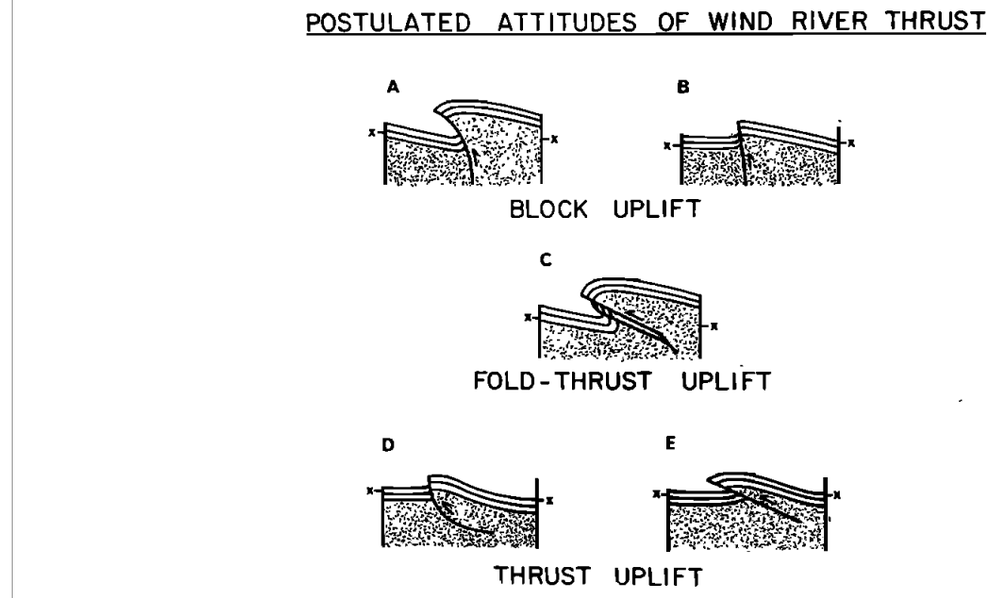

Fig. 1. Proposed structural styles for the Wind River fault. Structure between that in Figure 1c and in 1e is representative of the fault at depth; x-x represents the position of the present ground surface.

Smithson et al., JGR, 1979

Another approach helped to kill off the block uplift models—seismic reflection profiling.

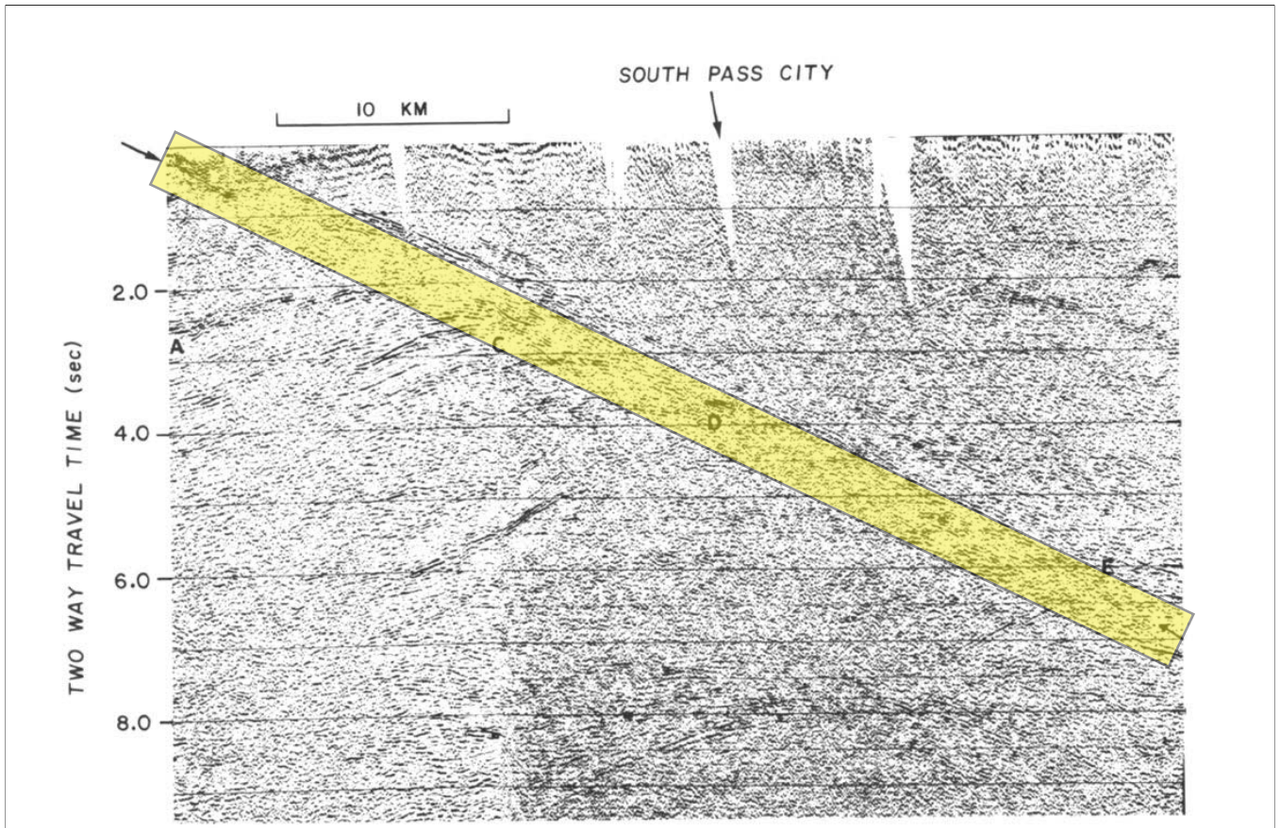

Figure 3. Unmigrated 24-fold CDP stacked reflection profile representing the upper portion of the Wind River thrust. Arrows define the position of the events representing reflections from the thrust plane. A = reflections from flat-lying sediments of Green River Basin. C = uplift (in line sections) of sedimentary reflectors under fault with no evidence of overturning. D = position of thrust against base of sediments. E = thrust reflection in the Precambrian crystalline rocks of the crust.

Smithson et al., Geology, 1978

COCORP line across Wind Rivers pretty thoroughly showed that the steep vertical faults were not present, instead dipping thrust faults.

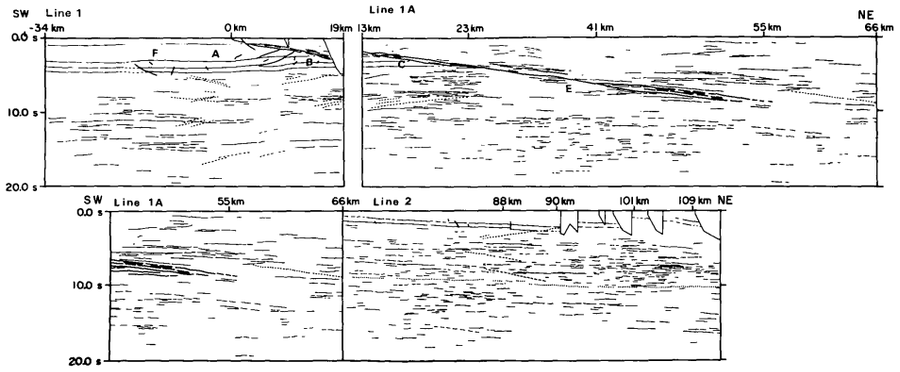

Figure 4. Interpretation of events seen on all three COCORP profiles. There is an overlap from the top northeast to bottom southwest parts of the diagram. The position of the Wind River thrust at the surface is represented by 0 km. The profiles were recorded to 20-s two-way traveltime. Dashed events represent diffractions or off-line reflections. A = reflections from flat-lying sediments of the Green River Basin. B = uplift (in time sections) of sediments underlying the Precambrian thrust over them by the Wind River thrust. C = termination of sedimentary layers against thrust with no evidence of overturning. E = appearance of thrust in the Precambrian crystalline rocks of the crust. Dotted lines represent enigmatic low-frequency event.

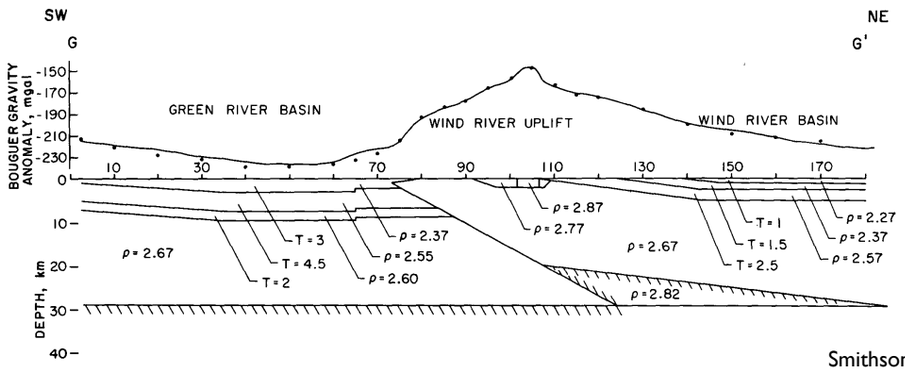

Smithson et al., Geology, 1978

Figure 5. Bouguer gravity anomalies and calculated model. Horizontal and vertical scale in kilometres. T = thickness of layers in kilometres; ρ = density in g/cm^3. Continuous line represents observed gravity. Dots represent modeled gravity.

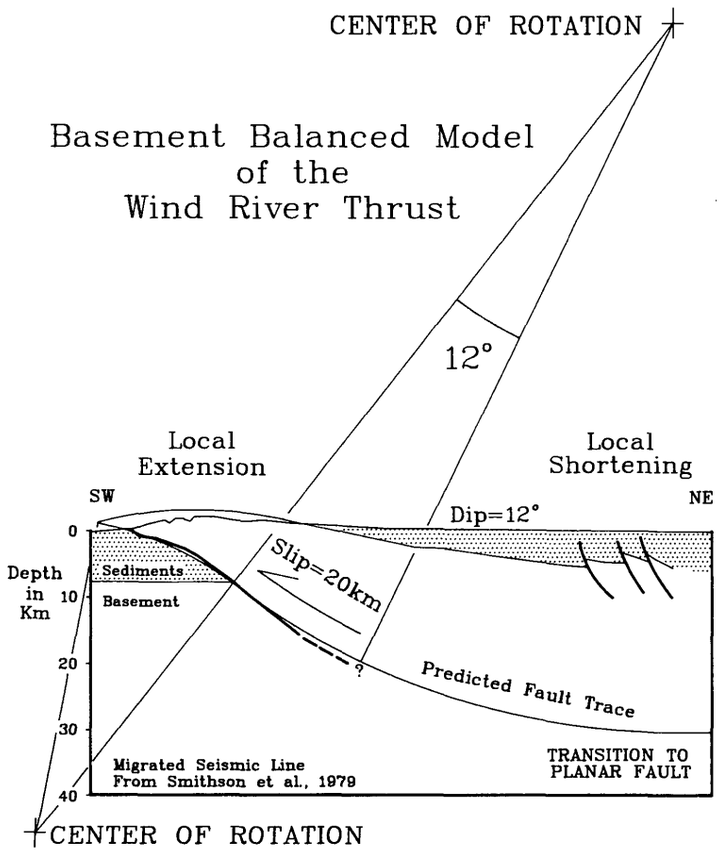

Figure 4. Illustration of congruency between seismic reflection data on Wind River thrust, Wyoming, and structural modeling discussed in text.

Erslev, Geology, 1986

Dip on backside of Wind Rivers demands some curvature on the fault…

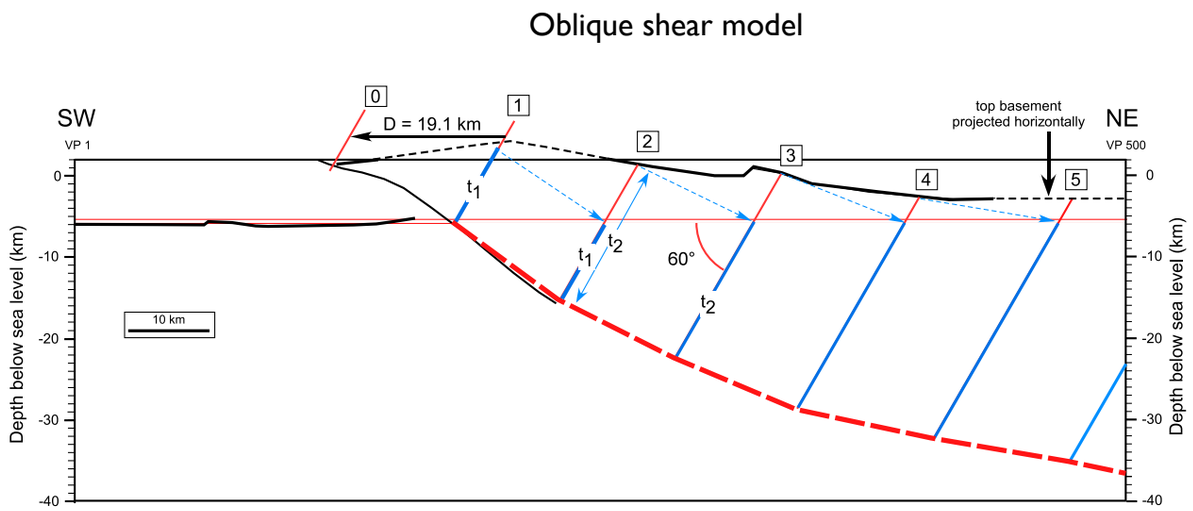

Figure 6. Explanation of oblique simple shear method applied to Wind River profile. The shear angle is 60° antithetic to the master fault. Shear lines are equally spaced according to the boundary displacement (D) and numbered 0–5, thicknesses t_1 and t_2 are along their respective shear lines, and thin dashed arrows show movement of thickness from original location to the regional.

Groshong and Porter, *Lithosphere*, 2019

The construction of the master fault is explained here in the context of the Wind River thrust (Fig. 6). Shear lines 0 and 1 are drawn through the hangingwall and footwall cutoffs of the master fault. The boundary displacement of the block (D) is the distance between these lines measured parallel to the regional. A set of shear lines is then constructed with spacing D. Line lengths between the marker horizon and the fault are measured, starting with t1, which is restored to its original position with the top at the regional on shear line 2. The base of t1 marks the location of the fault. Then t2 is measured, shifted to shear line 3 and the fault location marked at its base. This process is continued progressively across the profile to construct the complete fault. The shear lines can be as closely spaced as desired as long as the thicknesses are always shifted to the shear line a distance D away.

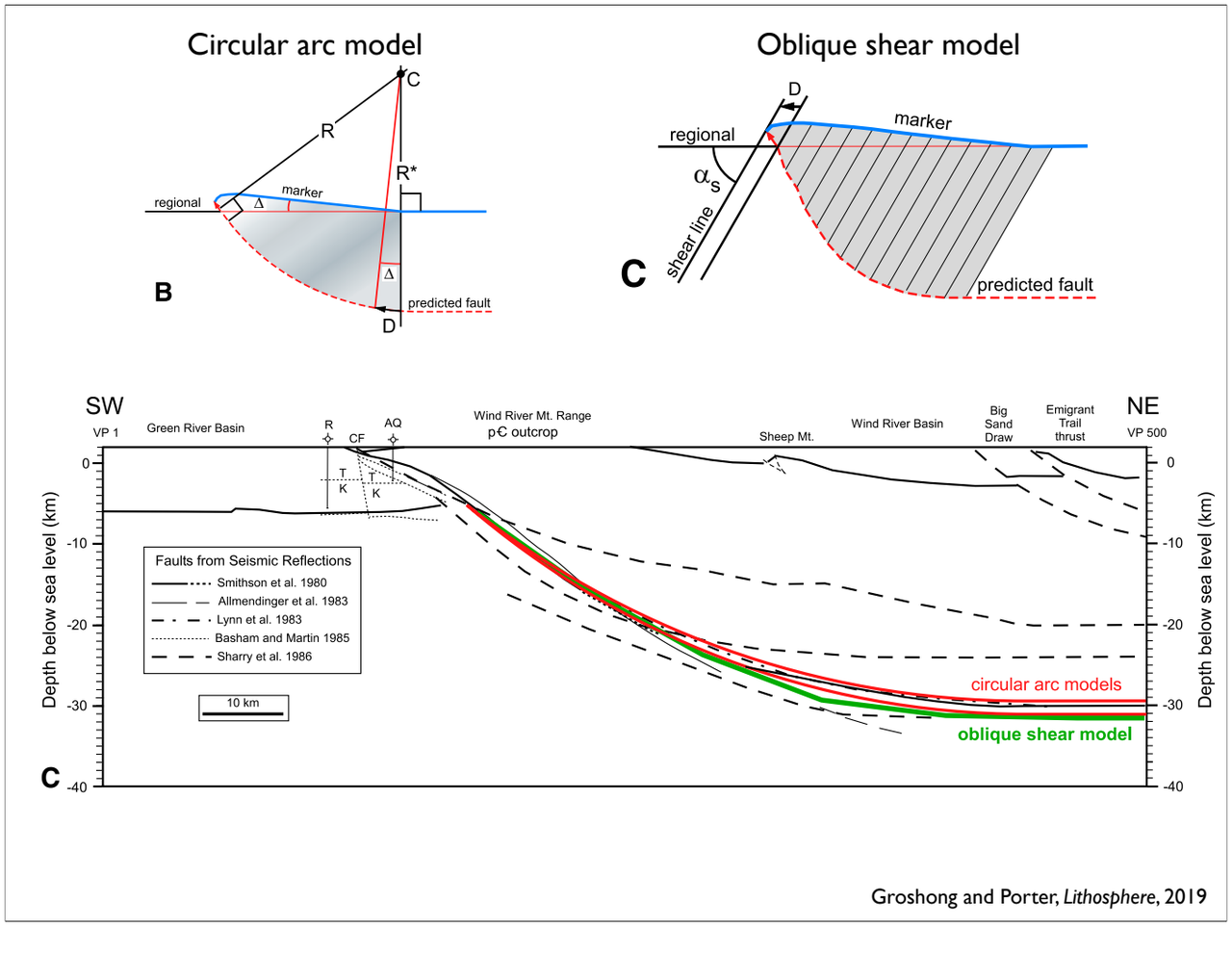

Groshong and Porter, *Lithosphere*, 2019

More recent analysis tends to confirm the circular arc approach (unlabeled red line is the final model determined in this paper). Note this paper puts Moho at 52 km, far below this horizontal fault. Displacements order 23 km pretty commonly inferred.

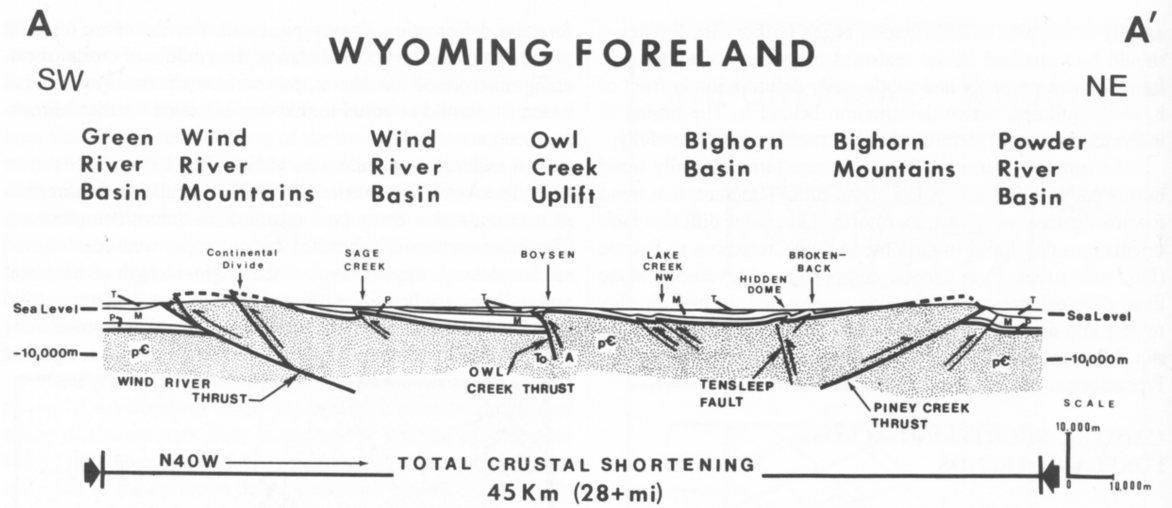

Figure 19. Regional true-scale structural cross section (line A-A′, Fig. 1) drawn parallel to direction of shortening and assumed direction of maximum compression (N.40°E.), demonstrates the conjugate nature of major foreland crustal faults. Different strike orientations of foreland structures result in differing amounts of crustal shortening, as shown by crossing the east-west–trending Owl Creek thrust and Tensleep fault, as compared to the northwest-trending Wind River thrust and the Piney Creek thrust in the Bighorn Mountains. Total crustal shortening along this line of section is 45 km (about 28 mi). T = Tertiary; M = Mesozoic; P = Paleozoic; p€ = Precambrian basement complex; To = toward; A = away.

Brown, GSA Mem 171, 1988

Other shortening estimates: 60-120 km by Chapin and Cather (1983) to NNE
43-52 km to ENE (Bird, 1998)

Given the Wind Rivers have 20 km themselves, 45 feels a bit short.

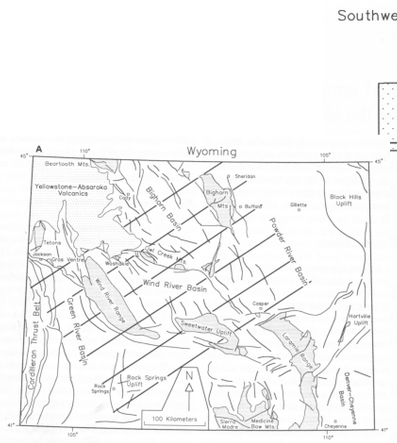

Figure 2. A: Structure map of Wyoming (after Blackstone, 1990a) with faults in finer lines and folds in thicker lines. Thick, broken straight lines show the cross-section lines for Figure 12. B: Arches and basins in Wyoming illustrating the connections between Rocky Mountain foreland culminations.

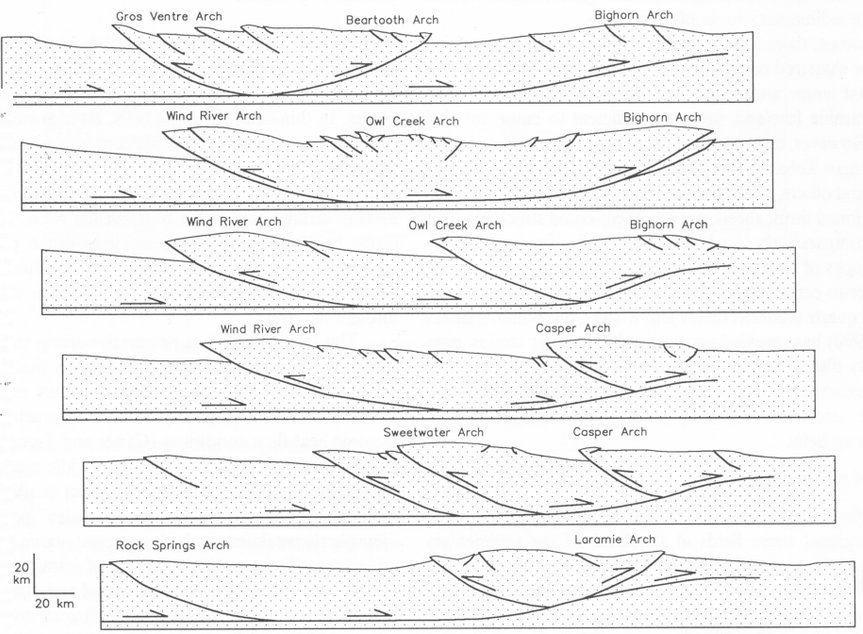

Figure 12. True-scale cross sections of the Precambrian basement surface in Wyoming (after Blackstone, 1990a) on lines shown in Figure 2A. These sections assume delamination in the lower crust and a uniform crust-mantle interface at 40 km below sea level. All fault geometries in the lower crust are schematic yet restorable in concept.

Erslev, GSA SP 280, 1993

What do these thrusts do at depth?

a) Case 1: Lithospheric fault blocks

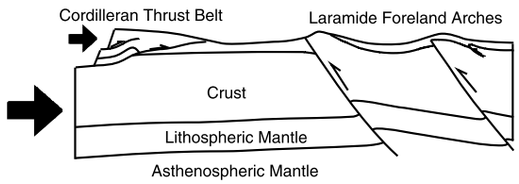

b) Case 2: Pure shear thickening

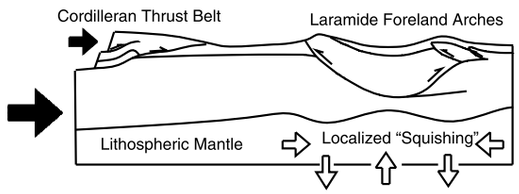

c) Case 3: Crustal detachment and buckling

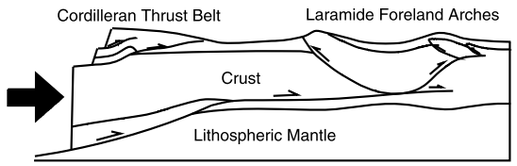

d) Case 4: Lithospheric buckling

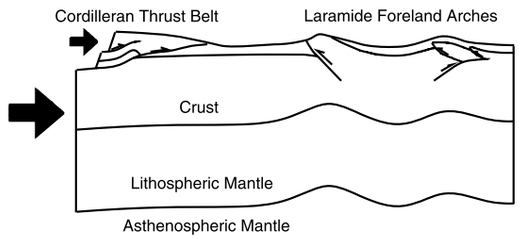

Yeck et al., JGR, 2014

What do these thrusts do at depth?

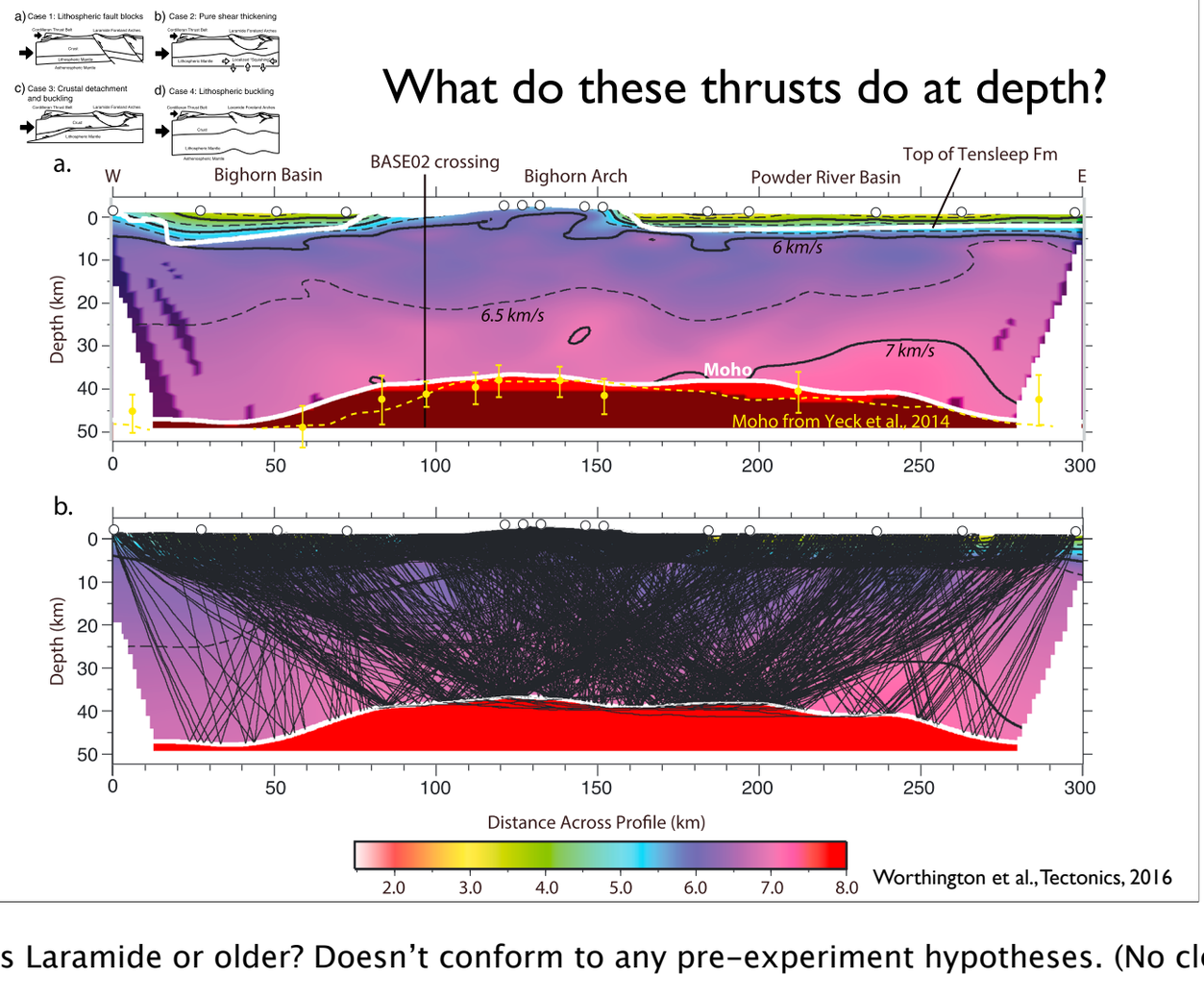

Worthington et al., Tectonics, 2016

The Moho is bowed up, it seems: is this Laramide or older? Doesn't conform to any pre-experiment hypotheses. (No clear reflections from faults were ever pulled out despite considerable effort).

What do these thrusts do at depth?

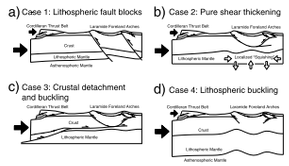

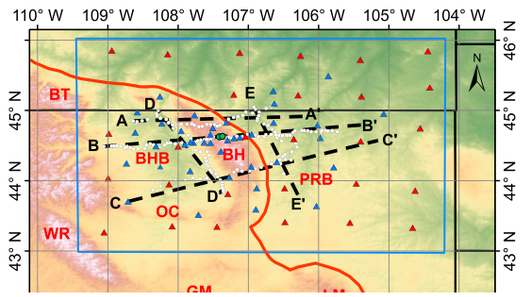

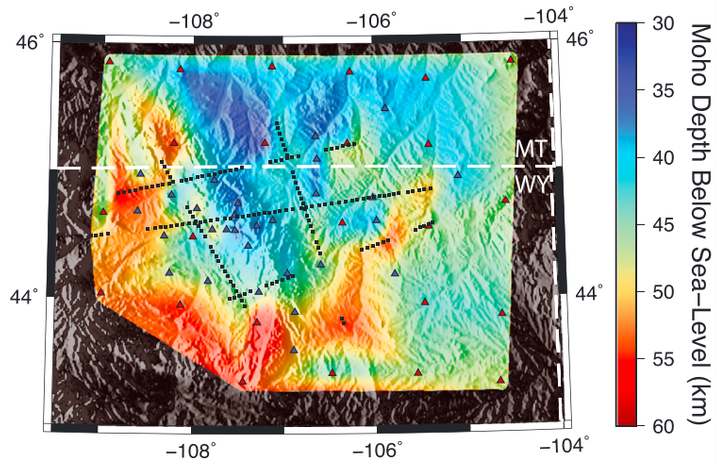

Yeck et al., JGR, 2014

Regional estimate of Moho little better—thin under Bighorns but also to NE. Owl Creeks to south might have far deeper Moho. So…confusion?

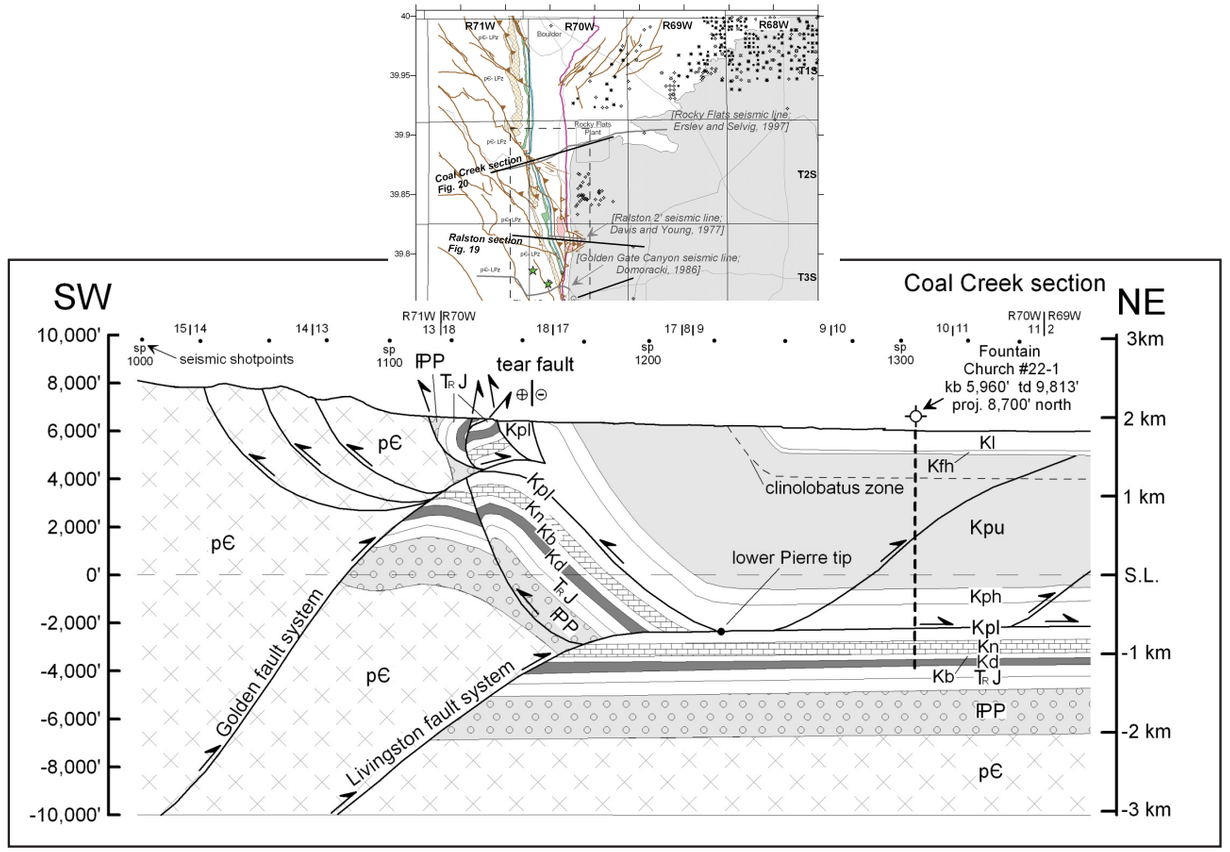

Sterne, Mtn Geologist, 2006

WHile the trishear models can be helpful, it seems that there are lots of complications.

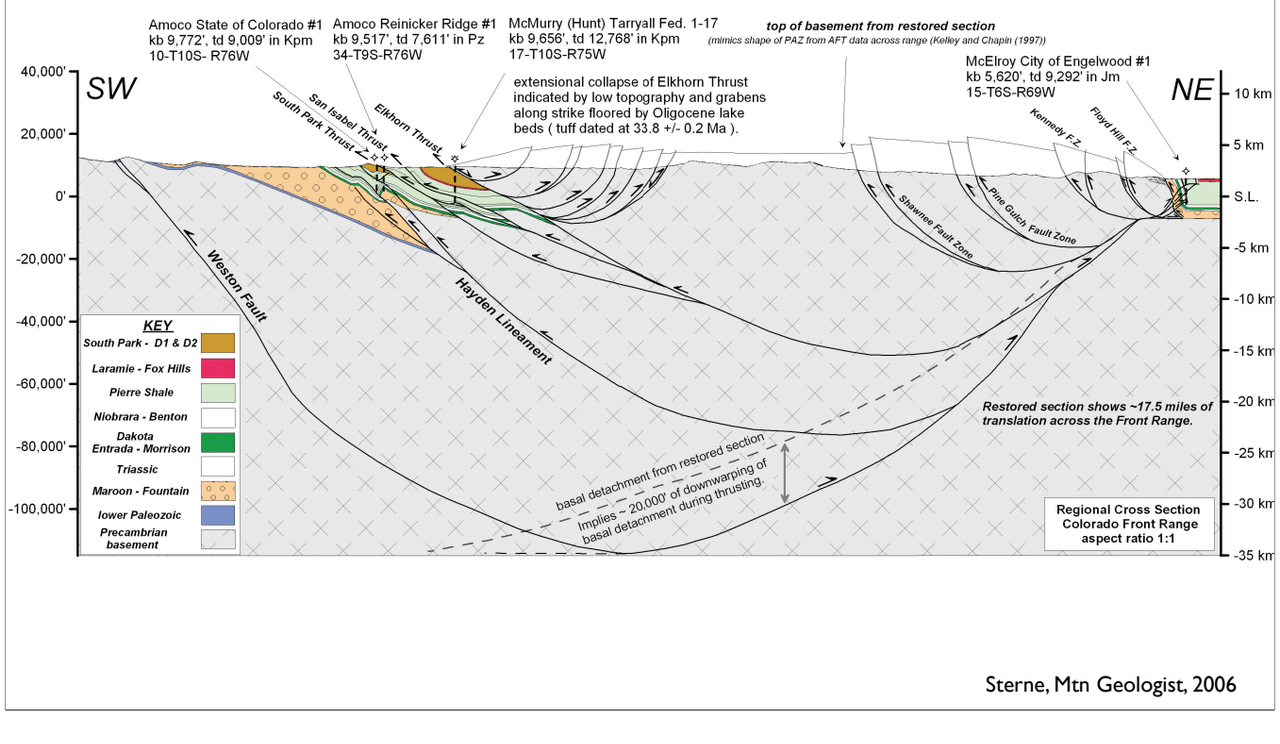

So this is a retrodeformable section in “thick-skinned” tectonics. Note the 17.5 mile (28 km) shortening across Front Range [but note, if shortening was oblique, movement was greater].

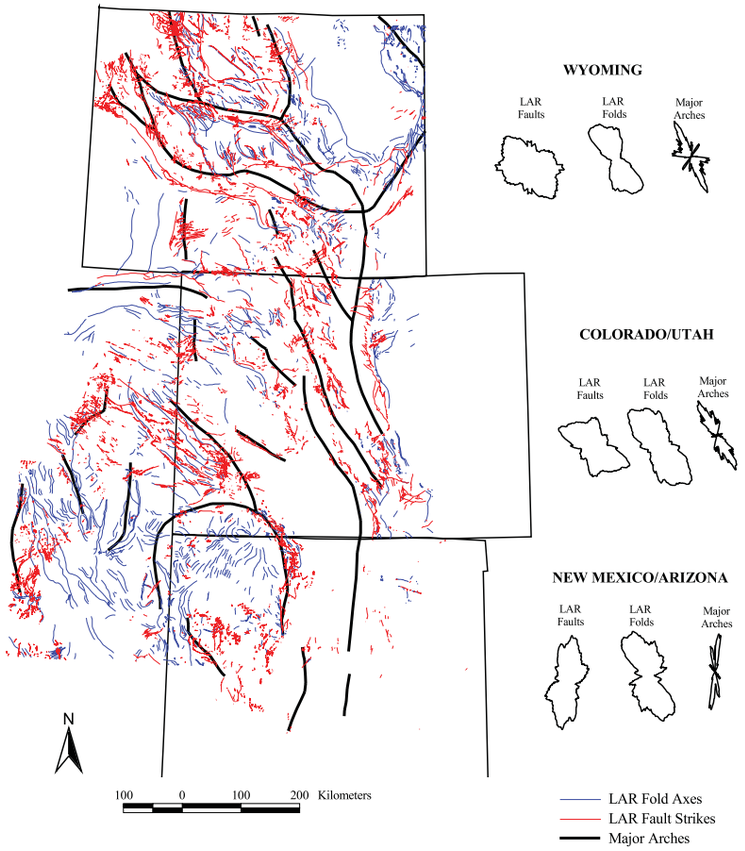

Figure 5. Map and rose diagrams of LAR arches, faults, and folds in Wyoming, Colorado-Utah, and New Mexico–Arizona.

Erslev, & Koenig, GSA Mem 204, 2009

Of course, you have to balance in proper shortening direction—which might be reflected in the geometry of folds and faults.

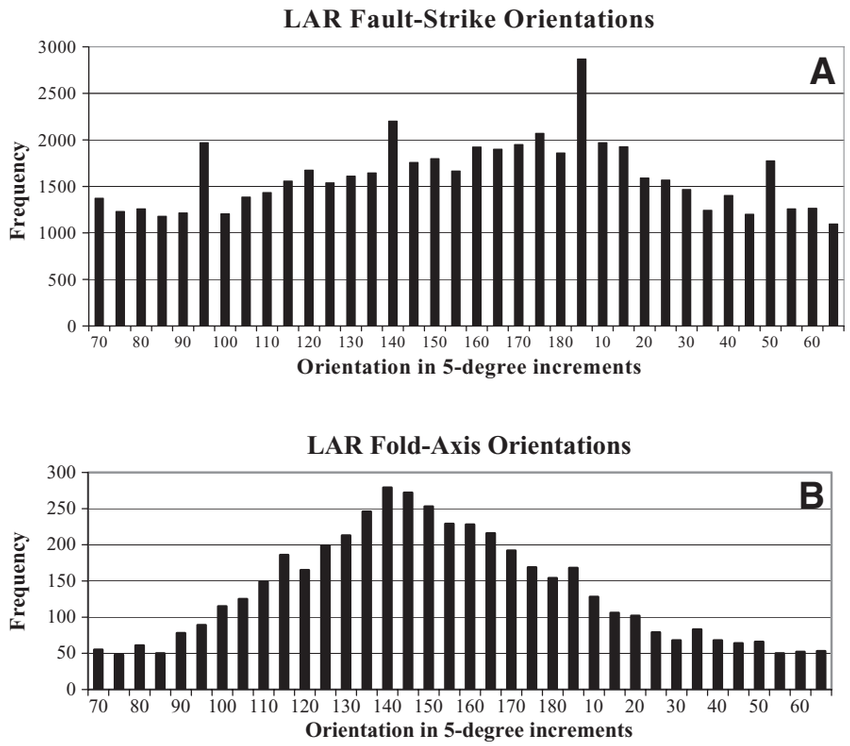

Figure 9. Histograms for all digitized LAR faults and folds from 0° to 180° in 5° increments.

Faults, curiously, show no bias, perhaps reflecting reactivation of all sorts of older structures. But folds do cluster near 140 (S40E), suggesting a N50E shortening direction.

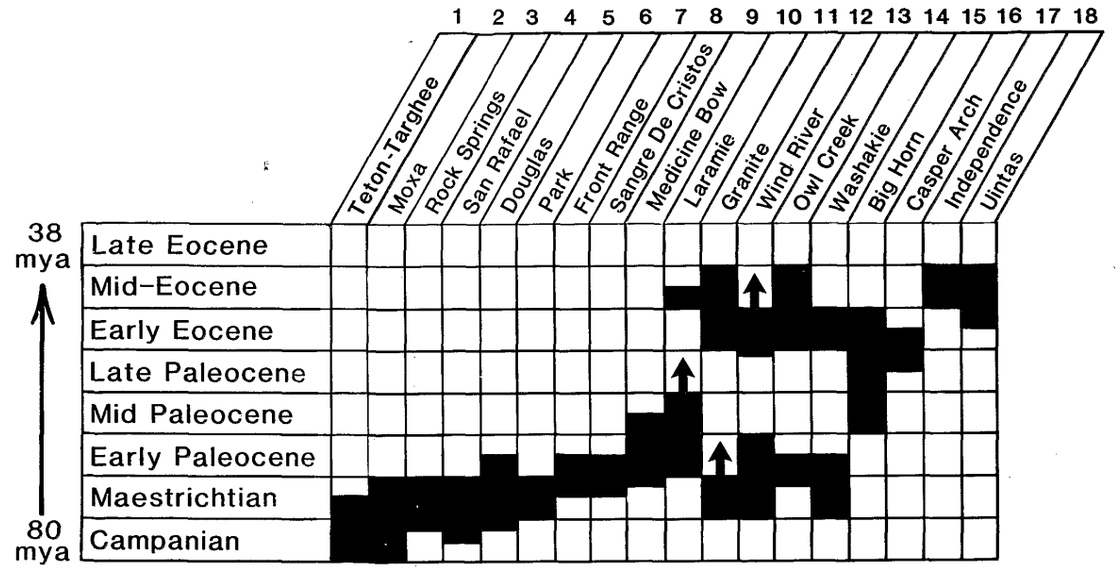

Figure 7. **Timing of uplift on Laramide ranges shows an early Laramide pulse of deformation (Campanian through middle Paleocene) and a late Laramide pulse (early and middle Eocene) separated by a late Paleocene lull.**

Gries, RMAG volume, 1983

Yet others had inferred two episodes of deformation with different orientations [and while I think the different orientations idea is fading out, the two times of shortening seems more resilient].

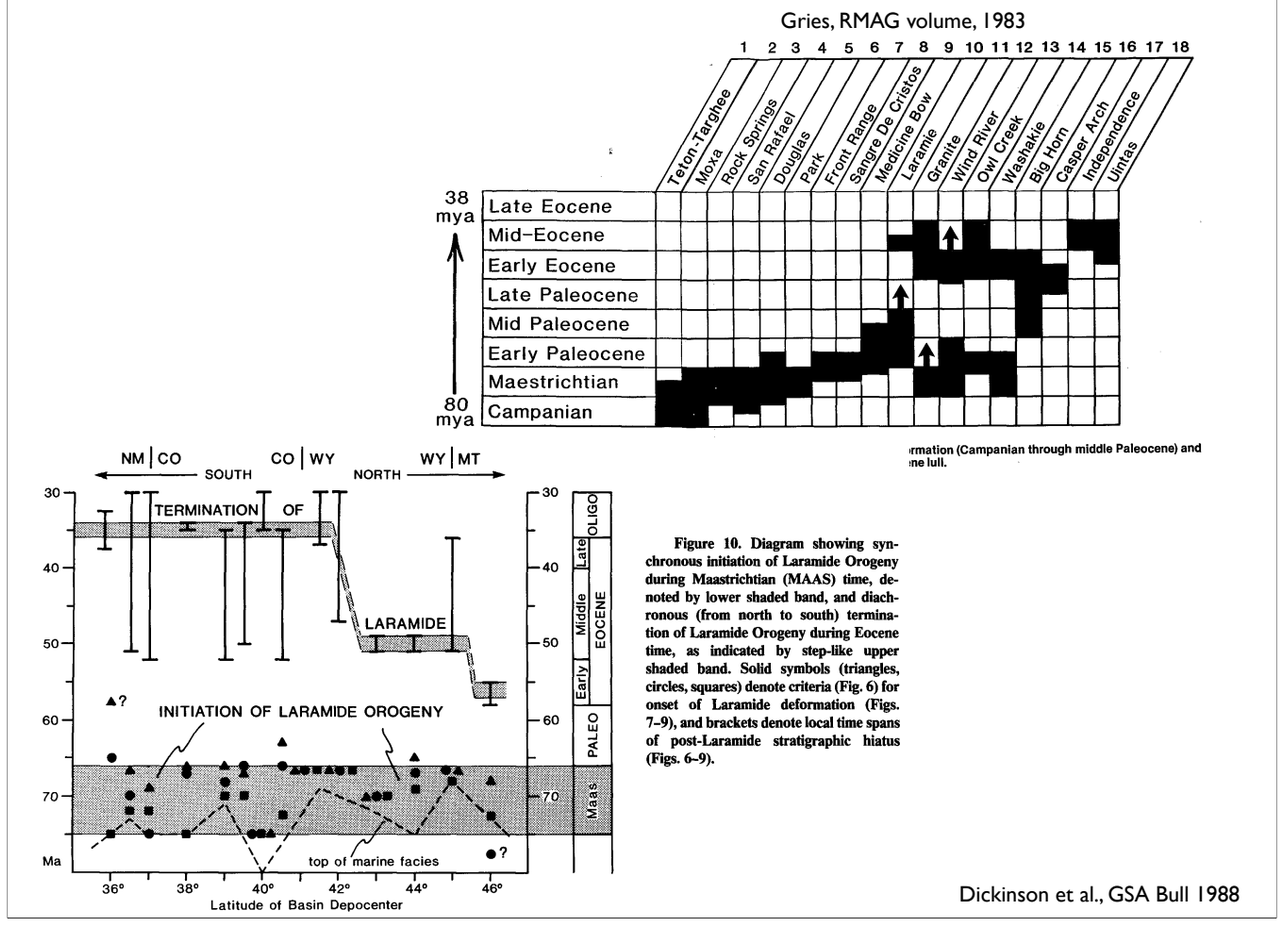

rmation (Campanian through middle Paleocene) and
ne lull.

Figure 10. Diagram showing synchronous initiation of Laramide Orogeny during Maastrichtian (MAAS) time, denoted by lower shaded band, and diachronous (from north to south) termination of Laramide Orogeny during Eocene time, as indicated by step-like upper shaded band. Solid symbols (triangles, circles, squares) denote criteria (Fig. 6) for onset of Laramide deformation (Figs. 7–9), and brackets denote local time spans of post-Laramide stratigraphic hiatus (Figs. 6–9).

Dickinson et al., GSA Bull 1988

There was disagreement on the timing, though…

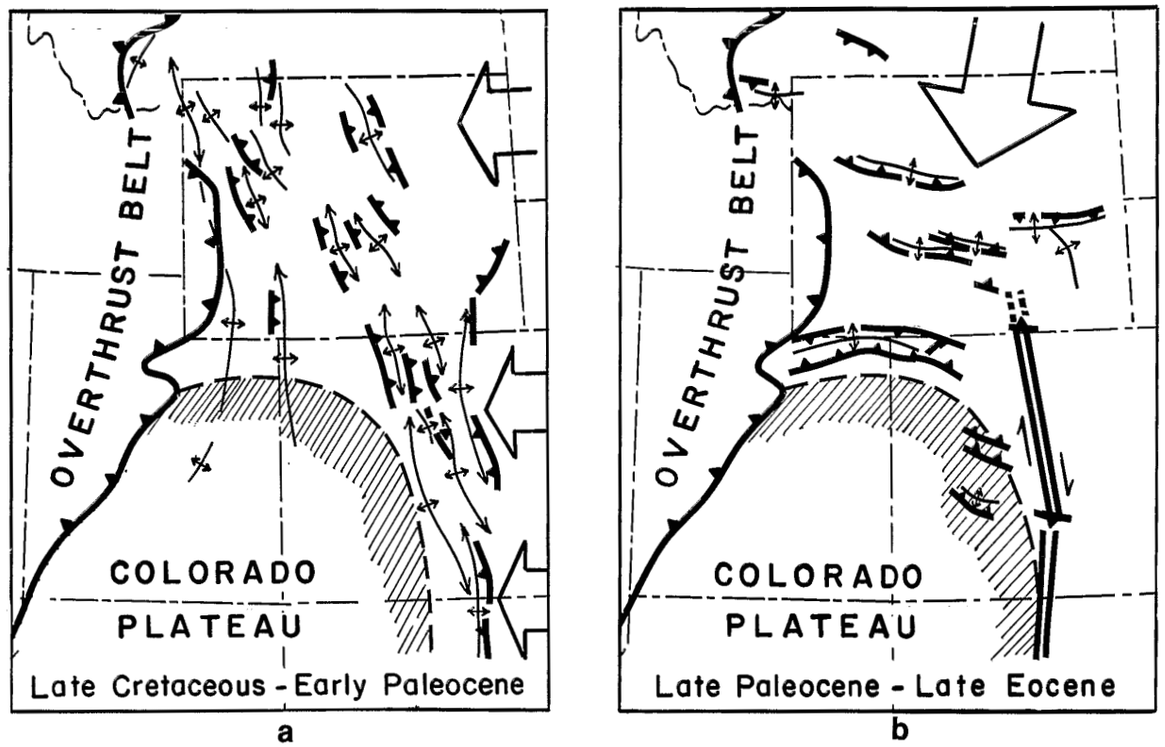

Figure 5. Timing and direction of compressional force related to the Colorado Plateau:
a. During early Laramide movement, uplifts and thrusts appear to be stacked along the east flank of the Colorado Plateau with broad arches plunging off to the north.
b. Late Laramide north-south compression caused formation of east-west-trending uplifts and basins from Montana to southern Colorado.

Gries, RMAG volume, 1983

How do we test ideas like this? After all, the ranges vary in strike. One approach is to determine the stress tensor consistent with observed deformation (an approach with a problem at its source, namely that the strain is quite finite, so stress no longer linear with strain).

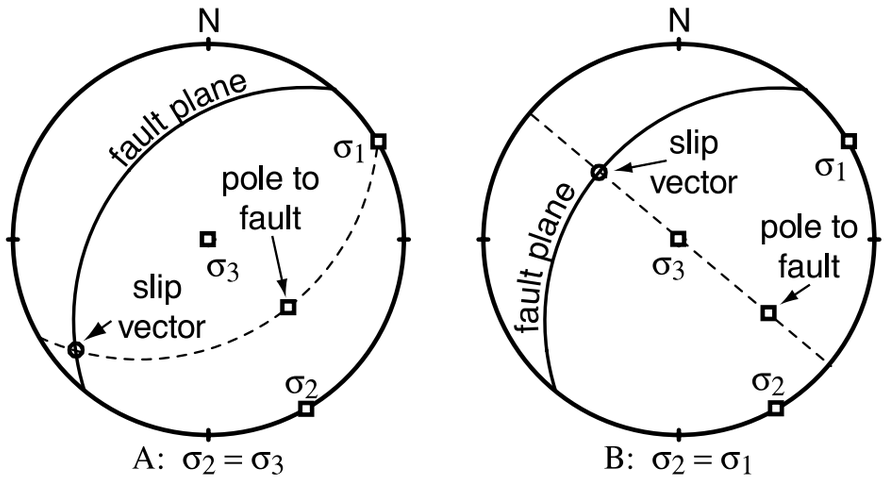

Figure 2. Illustration of the Angelier stereographic method for determining the direction of maximum resolved shear stress (and predicted slip) on a fault plane of given orientation [after *Angelier*, 1979]. Both Figures 2a and 2b are lower hemisphere projections showing the same fault plane and principal stress axes. (a) In the limit that σ_2 is equal in magnitude to σ_3 the slip vector is the line of intersection between the fault plane and the great circle that includes the pole to the fault and the σ_1 axis. (b) In the limit that σ_2 is equal in magnitude to σ_1 the slip vector is given by the intersection of the fault plane and the great circle that includes both the pole to the fault and the σ_3 axis. Intermediate σ_2 values predict slip directions between these two endpoints.

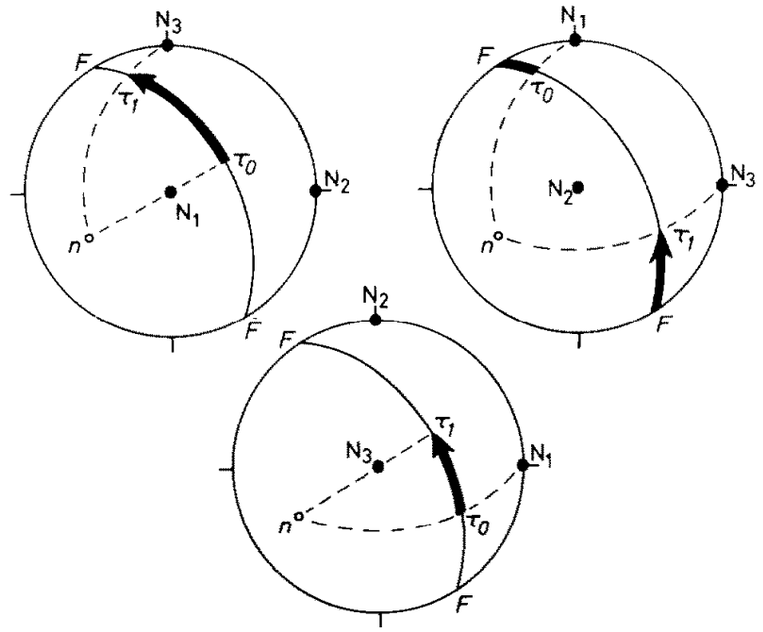

$$\Phi \equiv \frac{\sigma_2 - \sigma_3}{\sigma_1 - \sigma_3}$$

Fig. 4. Angular variation of shear stress with φ, when stress axes N_1, N_2, N_3 are fixed. n = perpendicular to fault plane F; τ_0 = projection of N_1 on F; τ_1 = projection of N_3 on F. When φ goes from 0 to 1, the shear stress goes from τ_0 to τ_1, travelling an angle δ (arrows), given by $\cos\delta = \tan\alpha_1 \cdot \tan\alpha_3$, where α_1 and α_3 are the angles of F with N_1 and N_3, respectively. Above, left: normal faulting. Above, right: strike-slip faulting (here dextral). Below: reverse faulting.

Angelier, Tectonophysics, 1979

In essence, shows how slip vector on a given plane maps to values of Φ (τ_0 is where phi is 0 ($\sigma_2=\sigma_3$), τ_1 is where phi is 1 ($\sigma_2=\sigma_1$)

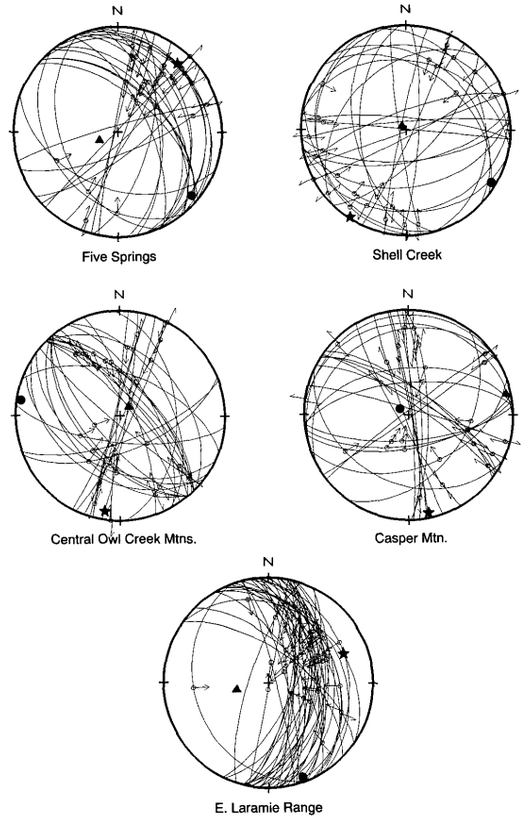

Figure 2. Lower-hemisphere, equal-area stereonets showing fault and tensor data for each site. Curved lines are cyclographic traces of individual fault surfaces, open circles indicate slickenside orientations on each fault, and full and half arrows show relative motions of fault hanging walls. Solid stars, triangles, and circles show orientations of σ_1, σ_2, and σ_3, respectively, as determined from tensor analysis of associated fault populations.

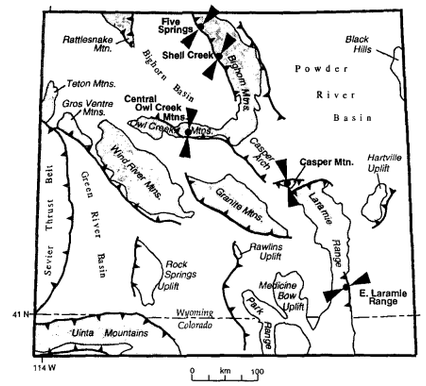

Figure 1. Map of central Rocky Mountain region showing principal Laramide foreland uplifts (patterned regions) and sites (solid circles) of paleostress analysis discussed in text. Large double arrowheads show direction of σ_1, determined at each site. Barbed lines adjacent to uplifts show positions of low-angle thrust faults as inferred from seismic data (e.g., Gries, 1983a) and from locations of monoclines.

TABLE 1. FAULT TENSOR DATA

			Principal Stress Axes				
	n	n*	σ_1	σ_2	σ_3	ϕ	T
Bighorn Mountains; Five Springs	28	27	040, 13	131, 7	248, 75	0.03	15
Bighorn Mountains; Shell Creek	26	24	212, 2	122, 4	329, 85	0.20	12
Central Owl Creek Mountains	32	27	188, 8	279, 6	045, 80	0.64	12
Casper Mountain	28	21	168, 6	306, 82	078, 6	0.15	21
East Laramie Range	40	37	068, 24	160, 4	259, 66	0.11	14

Note: Number of faults with known slip sense denoted by n; n* represents number of faults included in the final tensor solution. Principal stress axis orientations given as trend, plunge. Stress ratio $\phi = (\sigma_2 - \sigma_3) / (\sigma_1 - \sigma_3)$ from Angelier (1984). Importance of this ratio is questionable due to inclusion of both strike-slip and dip-slip faults in the tensor calculations. The average deviation (degrees) between measured striae and calculated traction vector is denoted by T.

Varga, Geology, 1993

Although the data as presented suggest range-normal shortening, the author ended up preferring a slip partitioned solution.

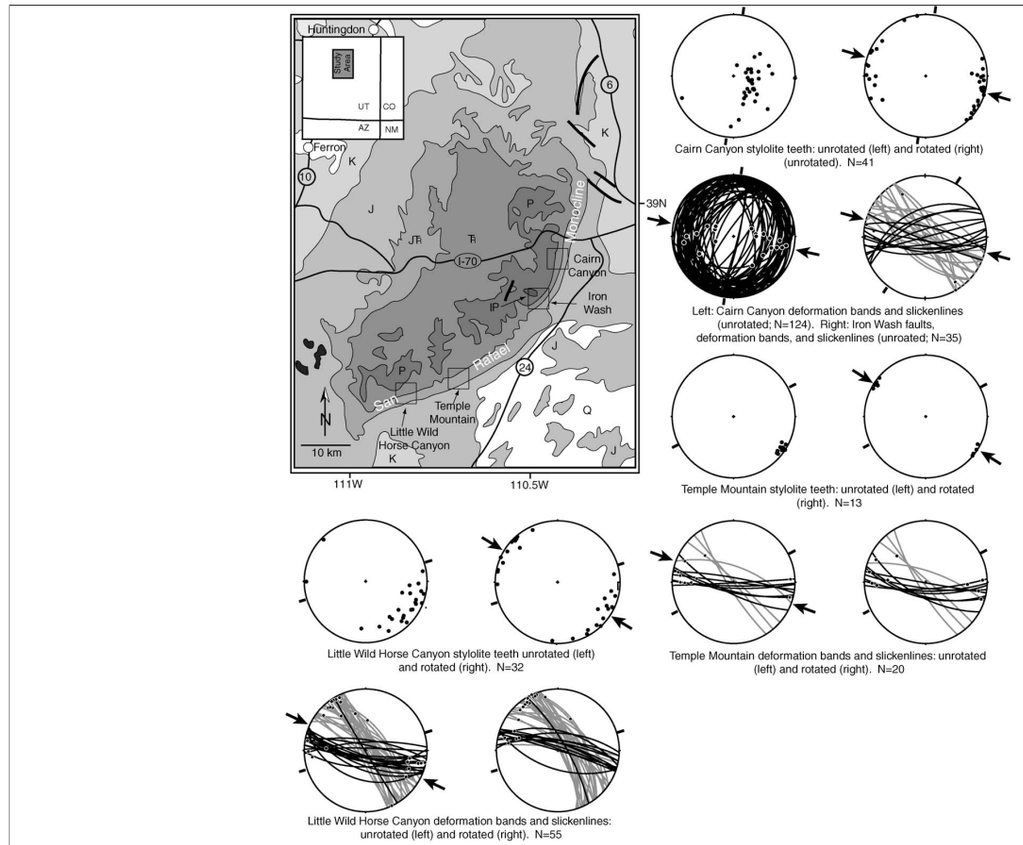

Fig. 7. Geologic map of the San Rafael Swell region (after Bennison, 1990) and lower hemisphere equal area stereoplots showing orientations of deformation bands, slickenlines and stylolite teeth. With the exception of deformation bands at Cairn Canyon and Iron Wash, orientations are shown both as measured ('unrotated') and rotated such that bedding is returned to horizontal ('rotated'). Strike-slip deformation bands (Iron Wash, Temple Mountain and Little Wild Horse Canyon) are shaded according to slip sense: left-handed deformation bands are shown in gray, right-handed ones in black. The Cairn Canyon area contains only reverse-slip deformation bands which are all shown in black. Paired arrows on each plot show the interpreted σ_1 direction based on the information within that plot. Paired heavy black tick marks on the outside of each plot show the local strike of the basement fault (which is assumed to parallel the strike of the monocline). Location map shows the area portrayed in Fig. 1.

Bump&Davis, J. Str. Geol., 2003

On the Colorado Plateau, get something different.

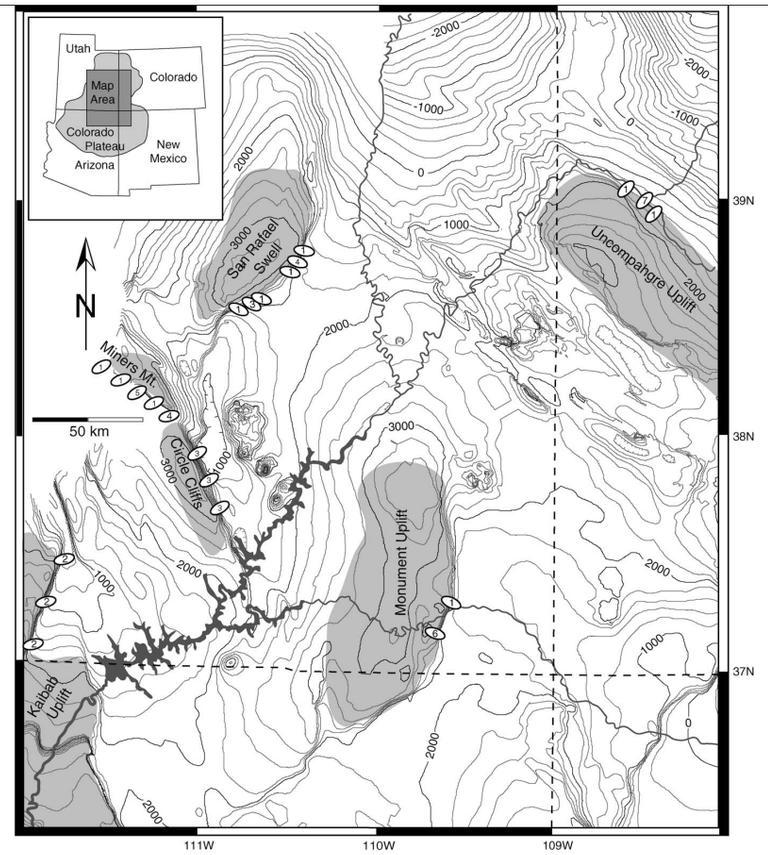

Fig. 11. Structure contour map of the northern Colorado Plateau showing the approximate areas of the uplifts (shaded gray) in this study. Contours are drawn at 200 m intervals on the base of the Cretaceous Dakota Sandstone (modified after Baker, 1935; O'Sullivan, 1963; Williams, 1964; Williams and Hackman, 1971; Haynes et al., 1972; Cashion, 1973; Hackman and Wyant, 1973; Haynes and Hackman, 1978). Structural elevations are in meters above sea level. Ellipses show local paleostress directions (though not magnitudes). Numbers inside ellipses refer to source of interpretation: 1. this study; 2. Tindall and Davis (1999); 3. Davis (1999), Anderson and Barnhard (1986), and Roznovsky (1998); 4. Davis (1999); 5. Anderson and Barnhard (1986); 6. Ziony (1966); 7. Jamison and Stearns (1982). The Colorado River and its tributaries are shown for reference in dark gray.

Bump&Davis, J. Str. Geol., 2003

Again, varying trends of structures—does this require multiple stress fields?

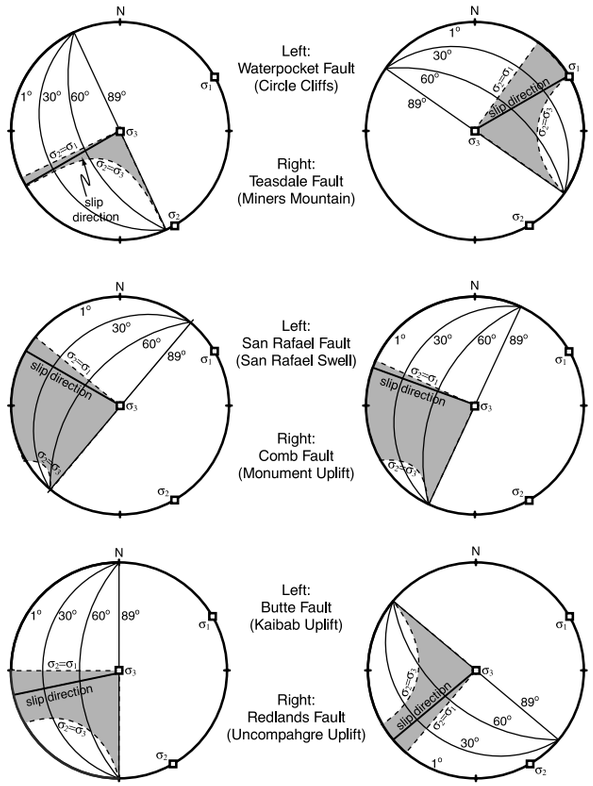

Figure 3. Lower hemisphere equal area projections of each of the six faults in this study, together with their interpreted slip trends, the range of possible orientations for the maximum resolved shear stress on the fault plane, and the principal stress axes. Because fault dips are poorly constrained, each projection shows four possible fault dips (labeled 1°, 30°, 60° and 89°) and all possible slip vectors that honor the geologically interpreted trend (solid black line labeled "slip direction"). The shaded region of each projection is the range of possible maximum resolved shear stress directions on the fault plane and is defined by the limits $\sigma_2 = \sigma_1$ and $\sigma_2 = \sigma_3$. The diagrams are most easily interpreted by plotting a fault of given dip and examining its overlap with the shaded region. High values of σ_2 will result in a slip vector close to the $\sigma_2 = \sigma_1$ limit while low values of σ_2 will produce slip vectors closer to the $\sigma_2 = \sigma_3$ limit.

Bump, Tectonics 2004

Bump seems to be suggesting that all these different slip vectors could be a single stress orientation with varying relative strength of sigma 2.

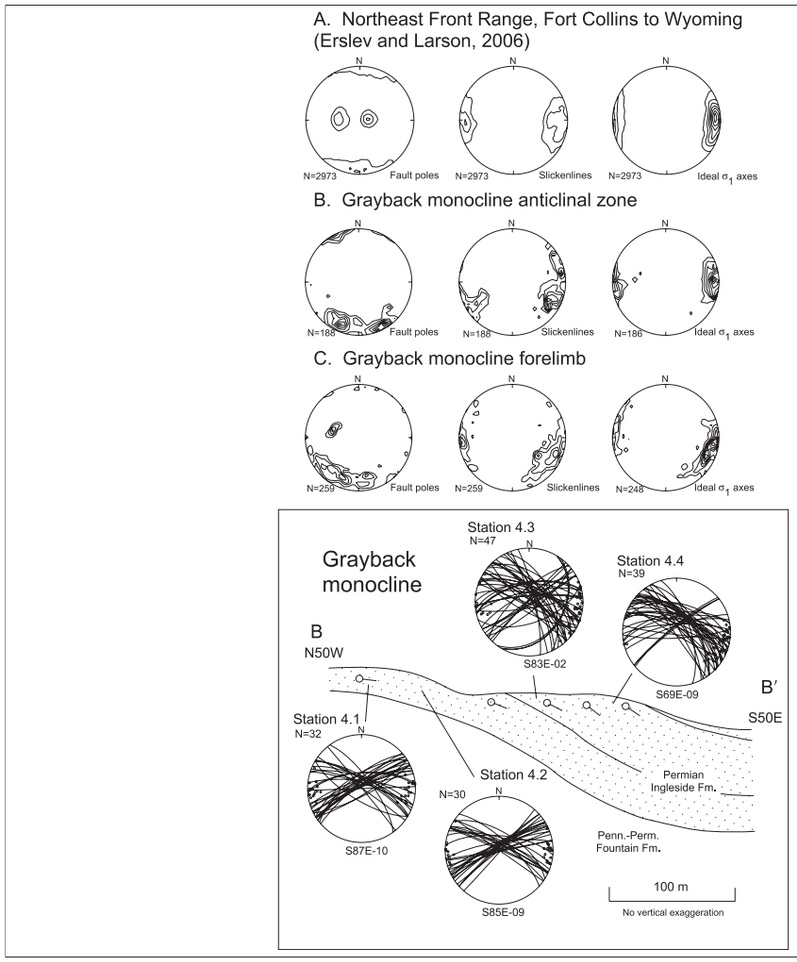

Figure 4. Lower-hemisphere, equal-area projection contour plots of structural data collected from this study with cross section B–B′ through the Grayback monocline along U.S. Highway 287 road cut. Fault data and cross section are from Erslev and Selvig (1997). All contour plots were made with the Schmidt method, using 40 nodes. The ideal σ_1 directions from the anticlinal zone (B) match well with the regional ideal σ_1 directions (A). However, the slickenlines and ideal σ_1 directions from the forelimb of the Grayback monocline (C) are deflected clockwise from the regional data. In the cross section, lower-hemisphere equal-area projection of fault planes (great circles) and ideal σ_1 directions (open circles) are plotted for stations 4.1–4.4. The compressive paleostress mean directions for each station in the cross section are given below the corresponding equal-area projection.

Tetreault et al., *GSA Bull.*, 2007

But there might be other complications out there. Perhaps more complex deformation.

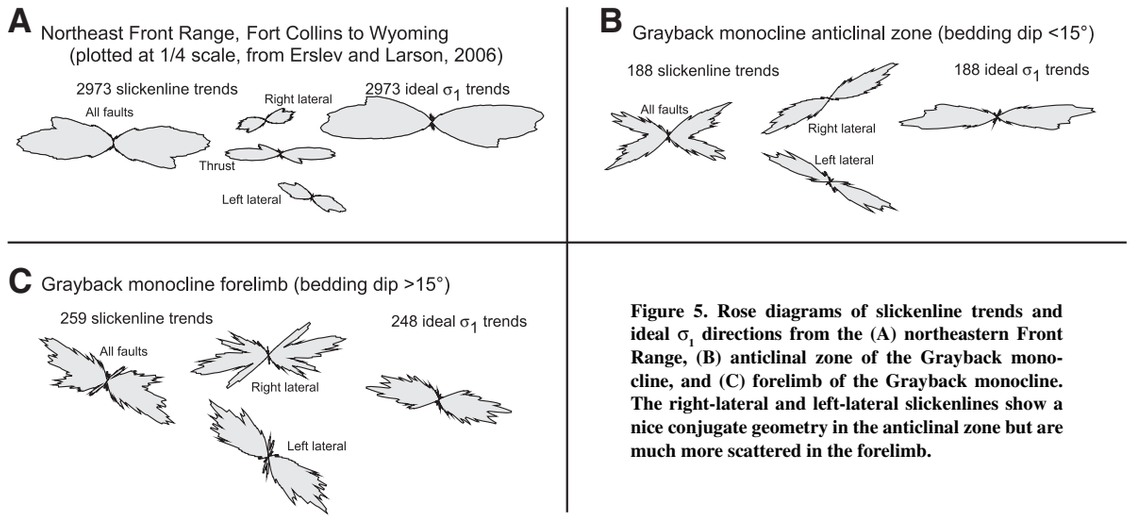

Figure 5. Rose diagrams of slickenline trends and ideal σ_1 directions from the (A) northeastern Front Range, (B) anticlinal zone of the Grayback monocline, and (C) forelimb of the Grayback monocline. The right-lateral and left-lateral slickenlines show a nice conjugate geometry in the anticlinal zone but are much more scattered in the forelimb.

Tetreault et al., *GSA Bull.*, 2007

Stresses in this fold depend on where in the fold you sample.

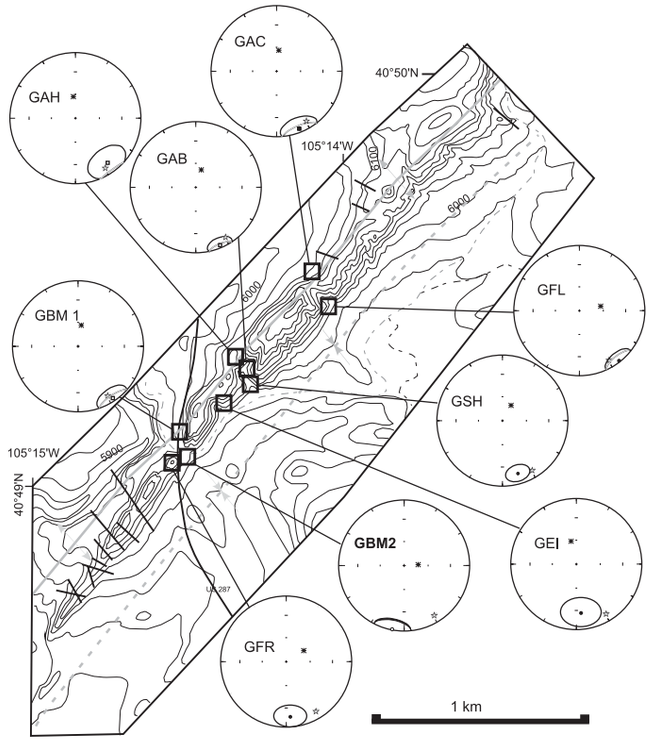

Figure 11. Topographic map (contour interval, 20 ft) of the Grayback monocline with equal-area plots of the tilt-corrected paleomagnetic results from analysis 1. See Figure 6 and caption for explanation of map symbols. Black circles represent lower-hemisphere Fisher locality mean directions, and open circles represent upper-hemisphere mean directions. Large circles around the mean directions represent the 95% circles of confidence. The star represents the expected Permian direction for the Ingleside Formation from Diehl and Shive (1979). Small black asterisks represent the tilt-corrected modern field directions for each locality. Localities in the anticlinal zone, GBM_1, GAC, GAH, and GAB, show no appreciable rotation. However, localities in the forelimb all show clockwise rotations, with the exception of GFL.

Tetreault et al., *GSA Bull.*, 2007

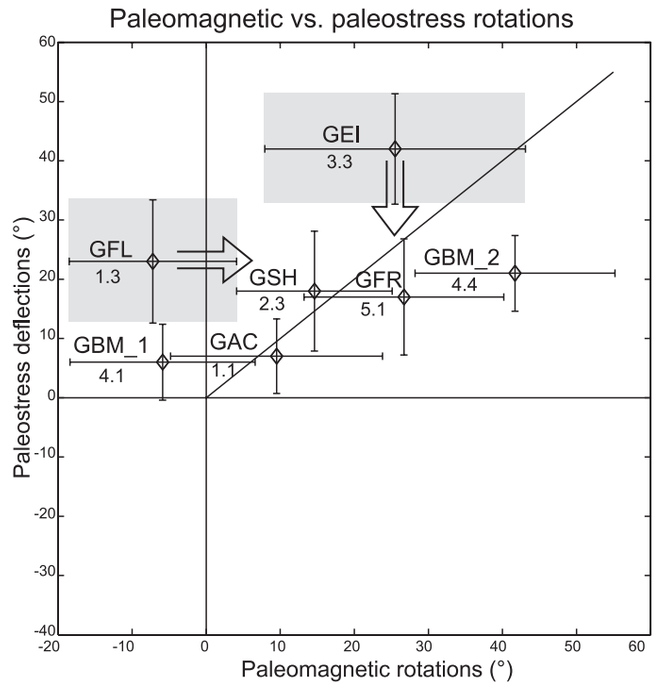

Figure 13. Vertical-axis rotations of paleomagnetic declinations versus compressive-paleostress deflections for spatially coincident stations and localities in the Grayback monocline. Error bars represent the 95% confidence level for vertical-axis rotation and station compressive paleostress deflection for each locality. A 1:1 trend line is shown for reference. Vertical-axis rotations are calculated relative to the Permian Ingleside Formation's declination of 149° (Diehl and Shive, 1979). Compressive paleostress deflections are calculated with respect to the regional compressional stress direction of N90°E (Erslev and Larson, 2006). Shaded symbols represent those stations or localities that either do not have well-constrained mean directions or do not exactly occupy the same sampling area. The large arrows indicate where we hypothesize these locality-station pairs to actually plot. Station 3.3 is located in steeper beds than paleomagnetic locality GEI, which lies between stations 3.2 and 3.3. Following the trends seen at other structural stations, locality GEI could be associated with a smaller compressive paleostress deflection than the observed deflection at station 3.3, as indicated by the downward-pointing large arrow. Locality GFL has an anomalous counterclockwise vertical-axis rotation, which we suspect to be a result of heavy overprinting (see text for discussion). Locality GBM_1 shows no statistically significant paleomagnetic rotation.

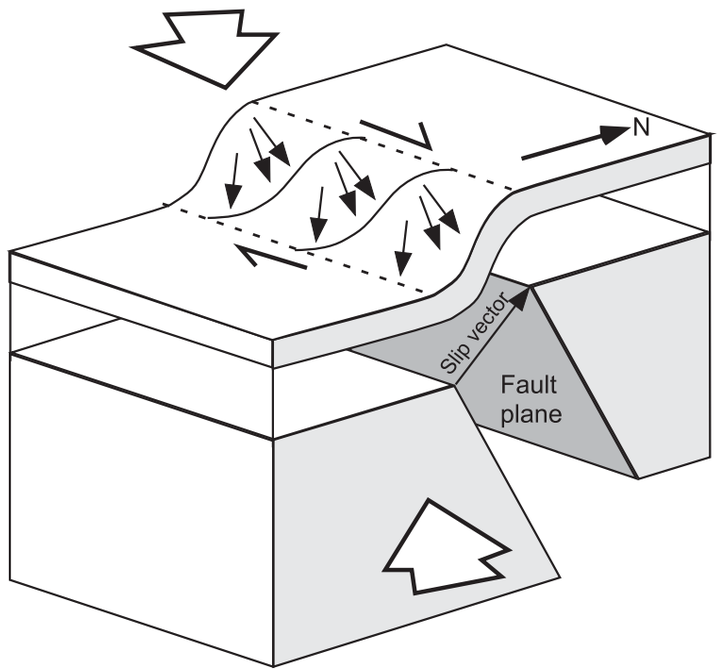

Figure 14. Cartoon depicting oblique-slip deformation in the folded strata of the Grayback monocline during the Laramide orogeny. The compressive paleostress and paleomagnetic rotations (depicted as arrows) are concentrated in the forelimb and increase with bedding dip. The regional shortening direction (large open arrows) is oblique to the fold trend.

Tetreault et al., *GSA Bull.*, 2007

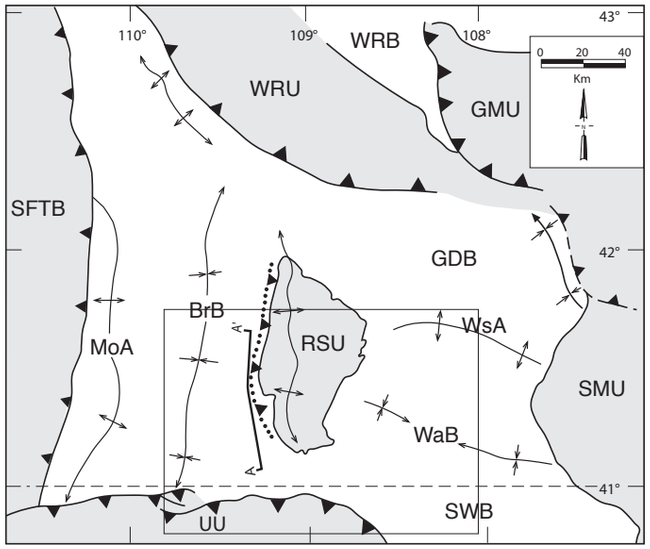

Figure 2. Map of the Greater Green River Basin and surrounding uplifts (modified from Lickus and Law, 1988). Abbreviations for uplifts: GMU, Granite Mountains; RSU, Rock Springs; SMU, Sierra Madre; UU, Uinta; WRU, Wind River. Abbreviations for sub-basins: BrB, Bridger; GDB, Great Divide; SWB, Sand Wash; WaB, Washakie; WRB, Wind River. Abbreviations for arches: MoA, Moxa; WsA Wamsutter. The Sevier fold and thrust belt is abbreviated as SFTB. Rectangle represents the area of Figures 5, 6, and 7. Cross section line A–A' is the location of Figure 4.

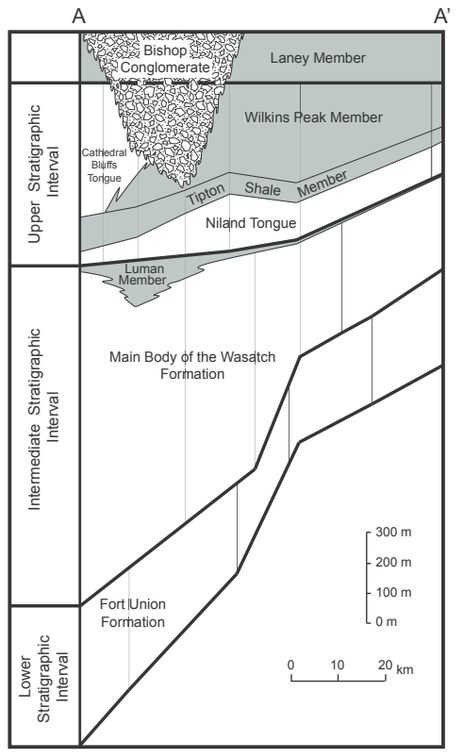

Figure 4. Cross section along the west flank of the Rock Springs uplift. Stratigraphic thickness data from Roehler (1961, 1965, 1973c, 1981) and Johnson (1990). The vertical lines rep-

Notice presence of north-south Rock Springs uplift near east-west Uintas and folds to east. Are these synchronous?

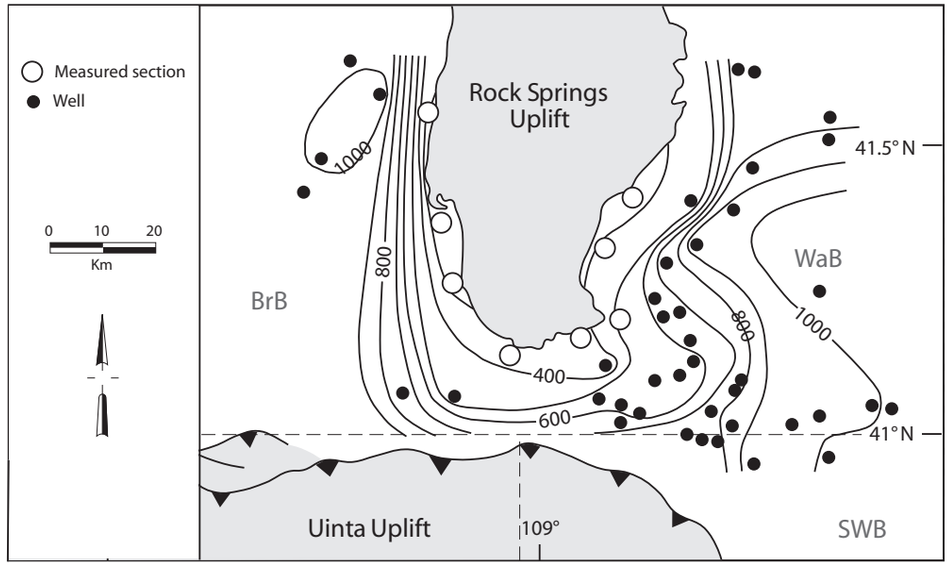

Figure 5. Isopach map of the lower stratigraphic interval (Paleocene). The contour interval is 100 m. Abbreviations for subbasins: BrB, Bridger; SWB, Sand Wash; WaB, Washakie. Stratigraphic thickness data from Roehler (1961, 1973a, 1973b, 1973c, 1974a, 1974b, 1974c, 1974d, 1977, 1979), McDonald (1975), Tyler, (1980), Kirschbaum, (1987), Johnson (1990), Hettinger and Kirschbaum (1991), and Finn and Johnson (2005).

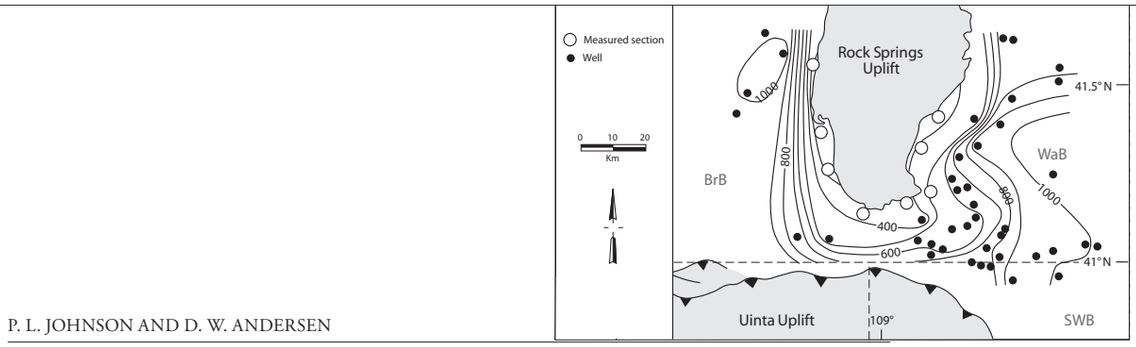

h map of the lower stratigraphic interval (Paleocene). The contour interval is 100 m. Abbreviations for sub-
SWB, Sand Wash; WaB, Washakie. Stratigraphic thickness data from Roehler (1961, 1973a, 1973b, 1973c,
, 1974d, 1977, 1979), McDonald (1975), Tyler, (1980), Kirschbaum, (1987), Johnson (1990), Hettinger and
nd Finn and Johnson (2005).

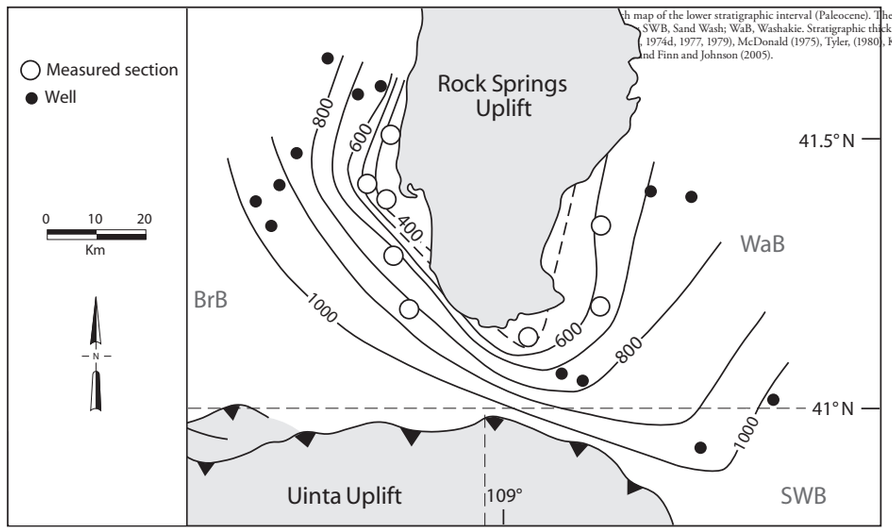

Figure 6. Isopach map of the intermediate stratigraphic interval (early Eocene). Stratigraphic thickness data from Roehler (1965, 1972, 1973a, 1974a, 1974d, 1979), McDonald (1975), Johnson (1990), and Finn and Johnson (2005).

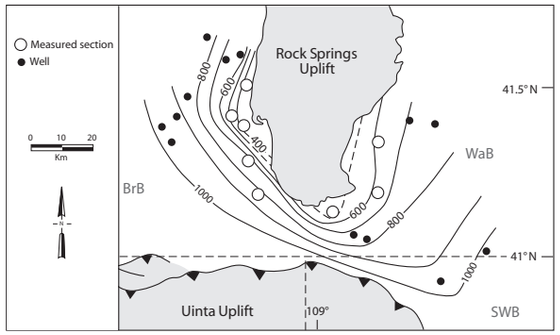

Figure 6. Isopach map of the intermediate stratigraphic interval (early Eocene). Stratigraphic thickness data from Roehler (1965, 1972, 1973a, 1974a, 1974d, 1979), McDonald (1975), Johnson (1990), and Finn and Johnson (2005).

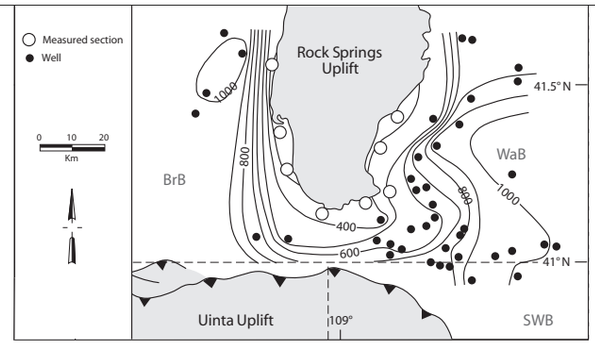

Figure 5. Isopach map of the lower stratigraphic interval (Paleocene). The contour interval is 100 m. Abbreviations for subbasins: BrB, Bridger; SWB, Sand Wash; WaB, Washakie. Stratigraphic thickness data from Roehler (1961, 1973a, 1973b, 1973c, 1974a, 1974b, 1974c, 1974d, 1977, 1979), McDonald (1975), Tyler, (1980), Kirschbaum, (1987), Johnson (1990), Hettinger and Kirschbaum (1991), and Finn and Johnson (2005).

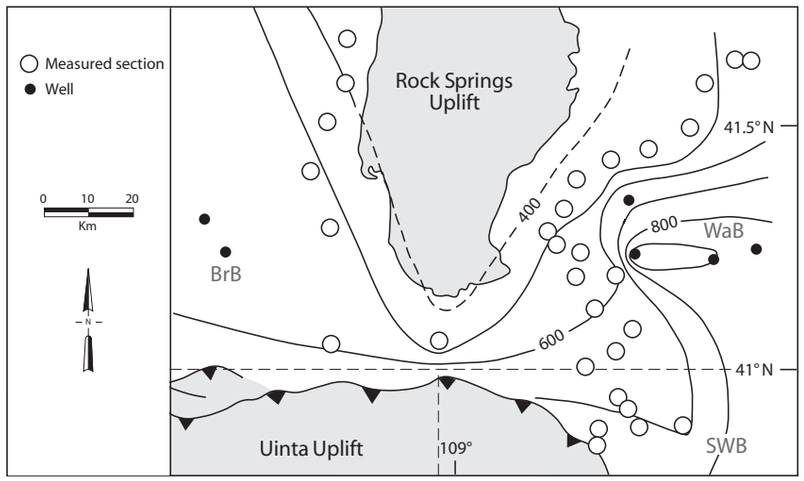

Figure 7. Isopach map of the upper stratigraphic interval (latest early and early middle Eocene). Stratigraphic thickness data from Colson (1969), and Roehler (1981, 1989, 1992).

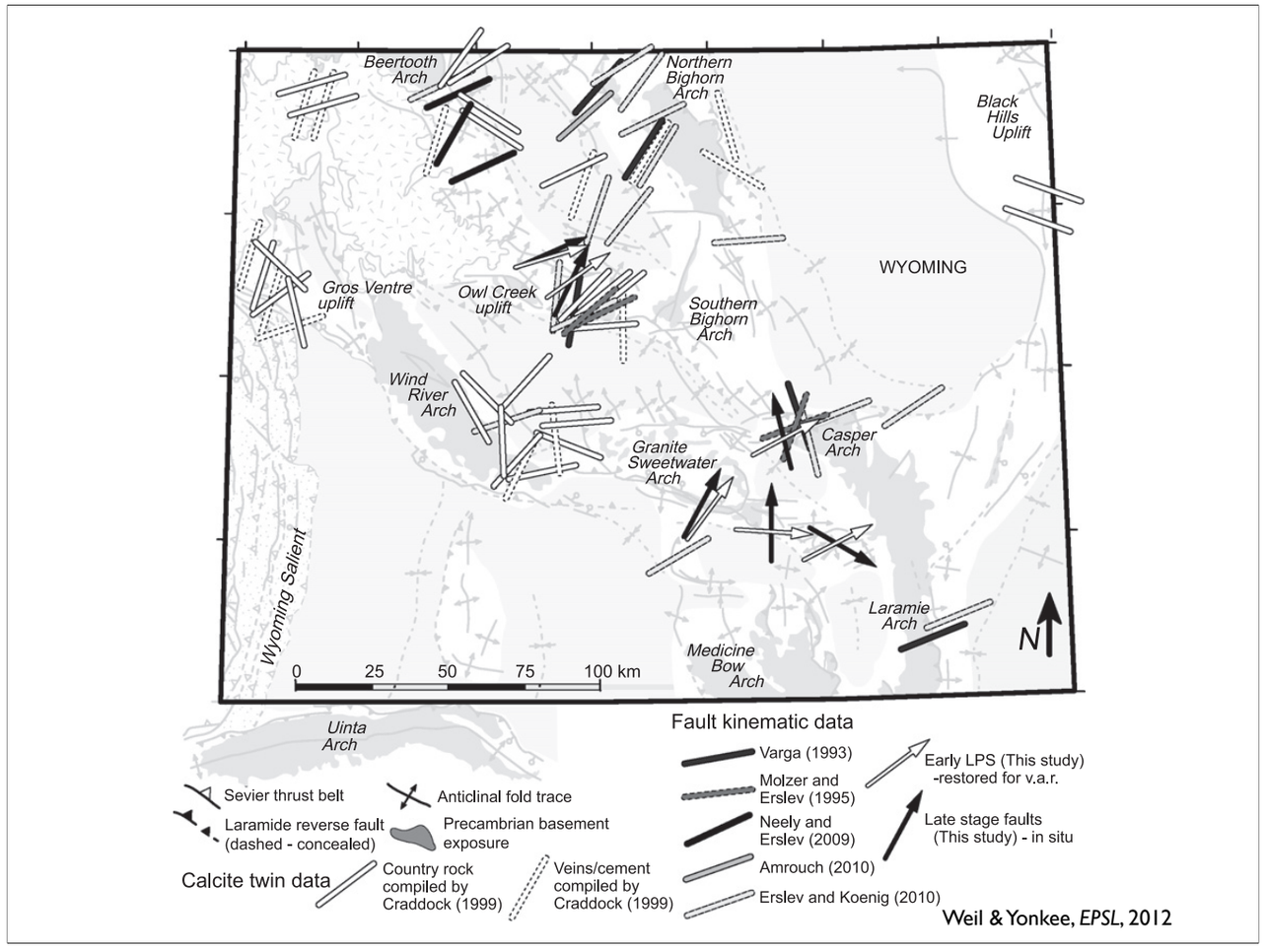

Pre-study estimates of fault kinematic data and early vs late fault slip--argue that the development of folds results in locally reoriented stresses and so these aren't robust indicators of regional shortening/stress field.

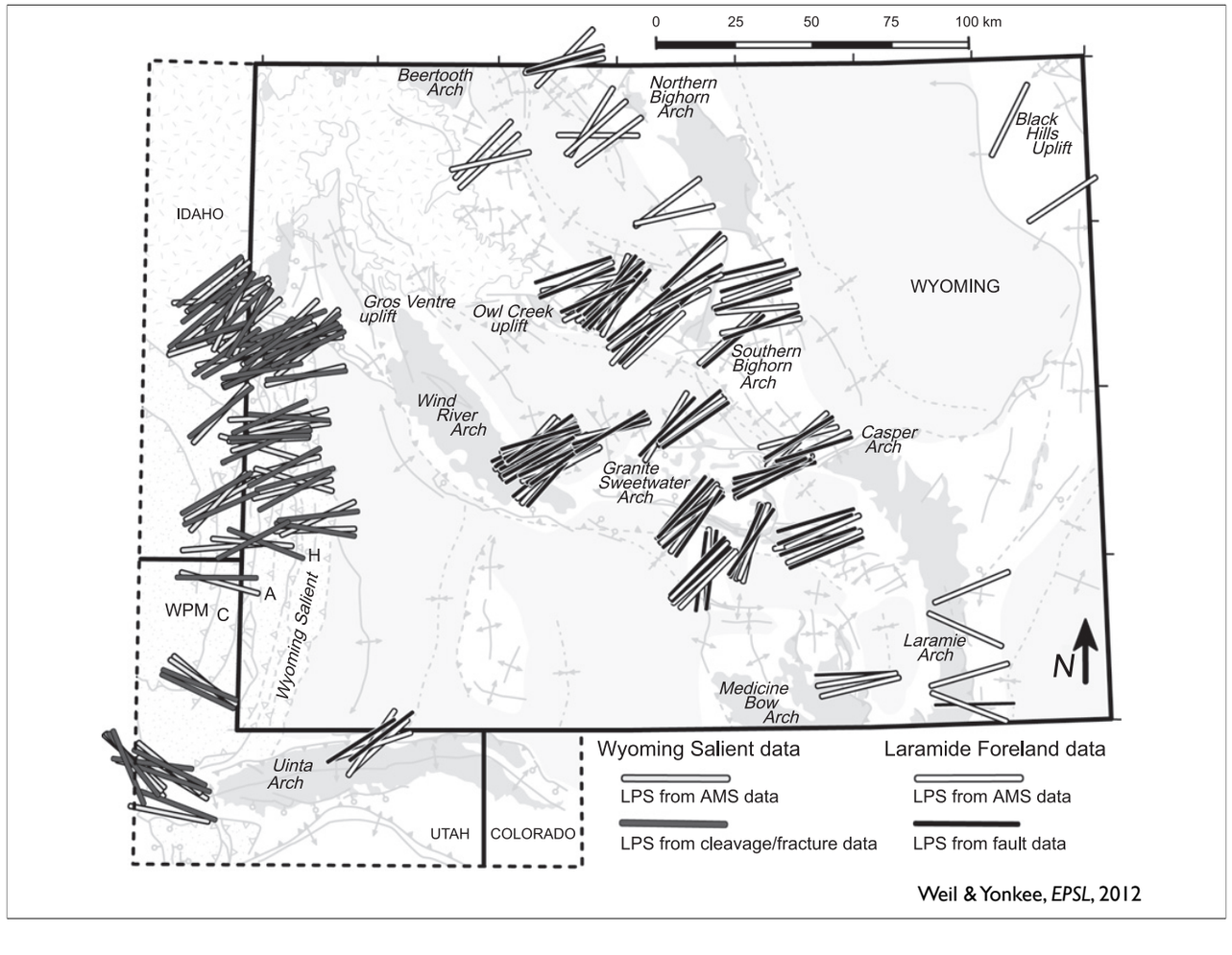

LPS is layer-parallel shortening. Stuff on the left is Sevier-style, center and right is Laramide-style

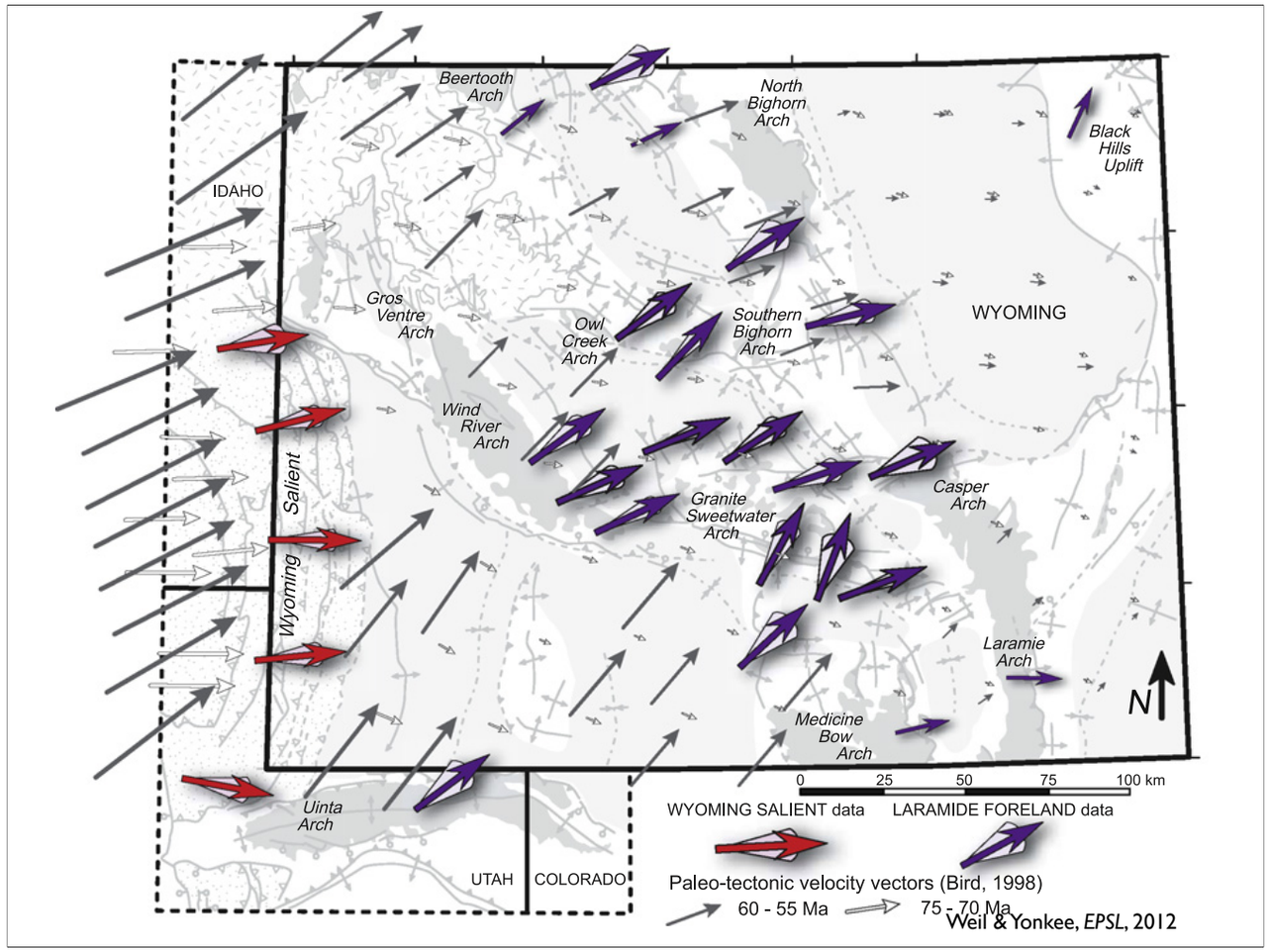
Beertooth Arch
North Bighorn Arch
Black Hills Uplift
IDAHO
Gros Ventre Arch
Owl Creek Arch
Southern Bighorn Arch
WYOMING
Wind River Arch
Salient
Wyoming
Granite Sweetwater Arch
Casper Arch
Laramie Arch
N
Medicine Bow Arch
0 25 50 75 100 km
WYOMING SALIENT data
LARAMIDE FORELAND data
Uinta Arch
UTAH
COLORADO
Paleo-tectonic velocity vectors (Bird, 1998)
60 - 55 Ma
75 - 70 Ma
Weil & Yonkee, EPSL, 2012

Comparison of all and inferred early stresses

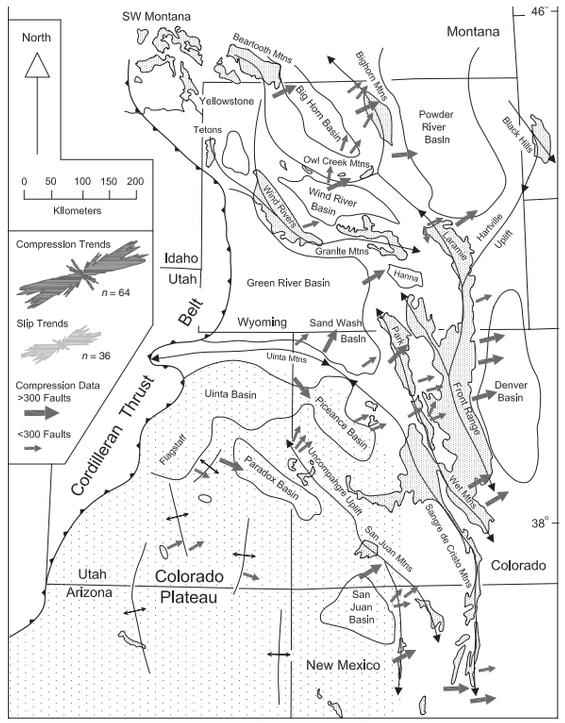

Erslev & Koenig, *GSA Mem 204* 2009

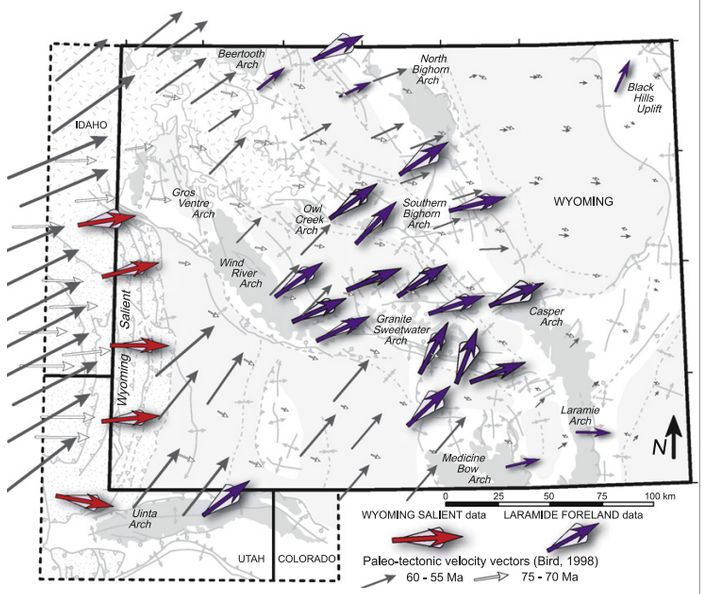

Weil & Yonkee, *EPSL* 2012

80-75 Ma

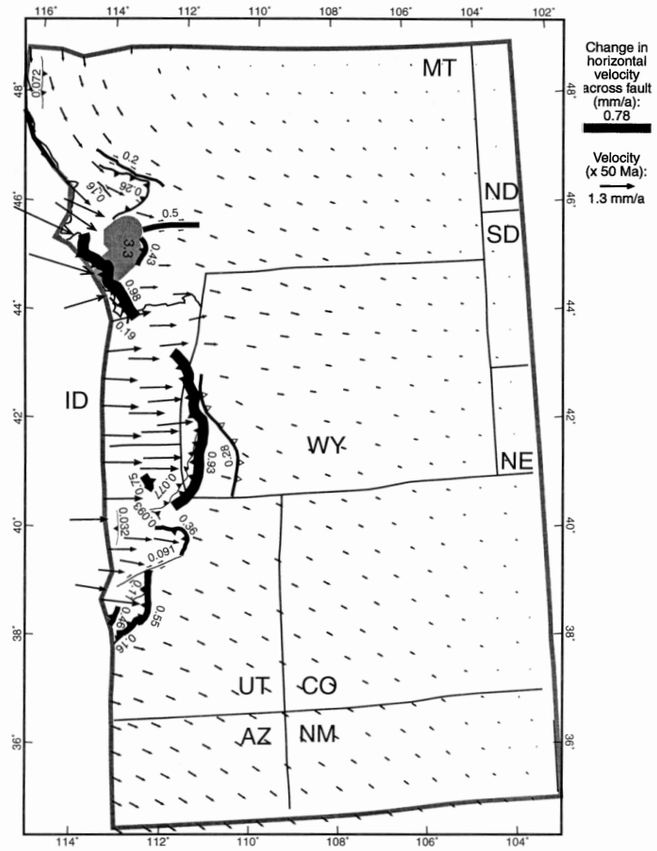

Figure 3. Paleotectonics during 80-75 Ma (Late Cretaceous: Campanian). Velocity vectors are relative to eastern North America. (Note that velocities are multiplied by 50 Ma, not 5 Ma, for legibility.) Width of fault traces is proportional to the magnitude of the horizontal component of the velocity change across the fault, and traces are labeled with this velocity change in mm yr^{-1}. (The fast moving Pioneer-Kelly-Grasshopper thrust in Montana is shown shaded to improve legibility.) State lines and grid outline are restored; latitude and longitude ticks in the margin show the undeformed reference frame of eastern North America. At this

Bird, Tectonics, 1998

75-70 Ma

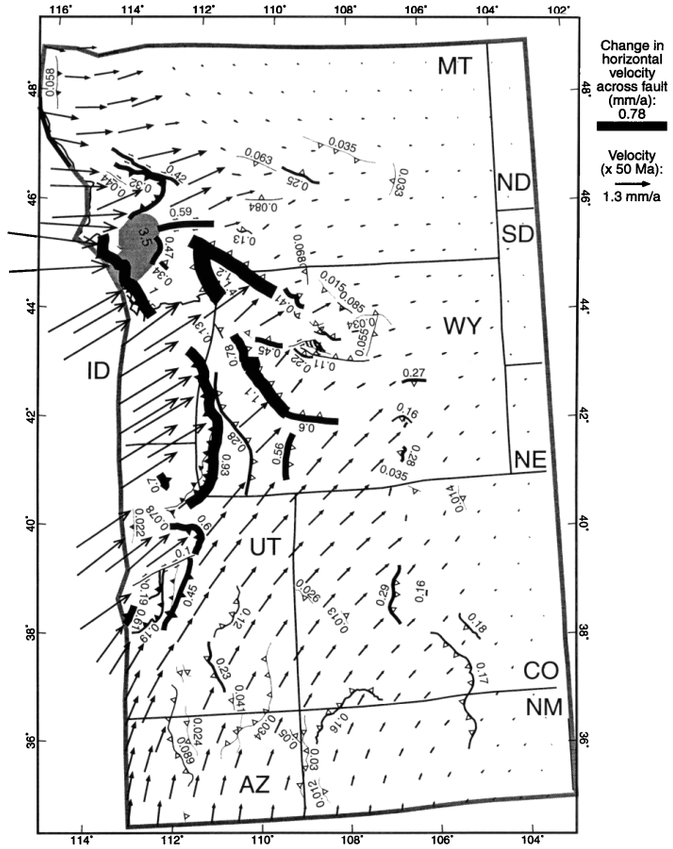

Bird, Tectonics, 1998

Figure 4. Paleotectonics during 75-70 Ma (Late Cretaceous: Campanian-Maastrichtian). Conventions are as in Figure 3. The Sevier orogeny continues. In this earliest part of the Laramide orogeny, activity was centered in western Wyoming but also spread south to central Colorado-New Mexico and north to central Montana. (The age of monoclines in the Colorado Plateau is poorly known; therefore these structures have similar activity in all time steps until 35 Ma.)

60-55 Ma

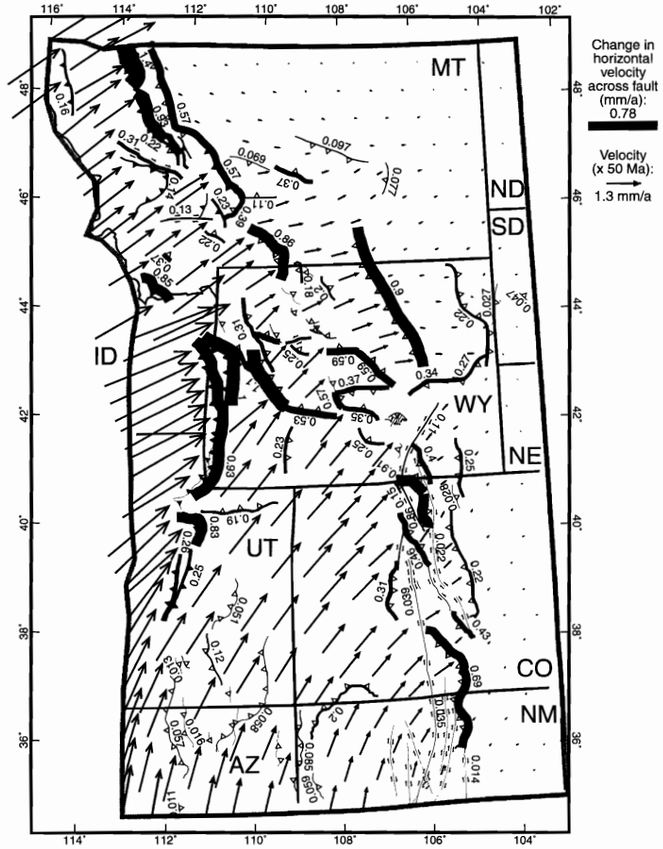

Bird, Tectonics, 1998

Figure 5. Paleotectonics at 60-55 Ma (late Paleocene-early Eocene). Conventions are as in Figure 3. This is the time of highest mean velocity in the Rocky Mountain foreland and Colorado Plateau. Laramide shortening in all regions (eastward to the Black Hills of South Dakota) was simultaneous with late Sevier orogeny in the western parts of the region. Note the rotational component of the motion of the Colorado Plateau.

45-40 Ma

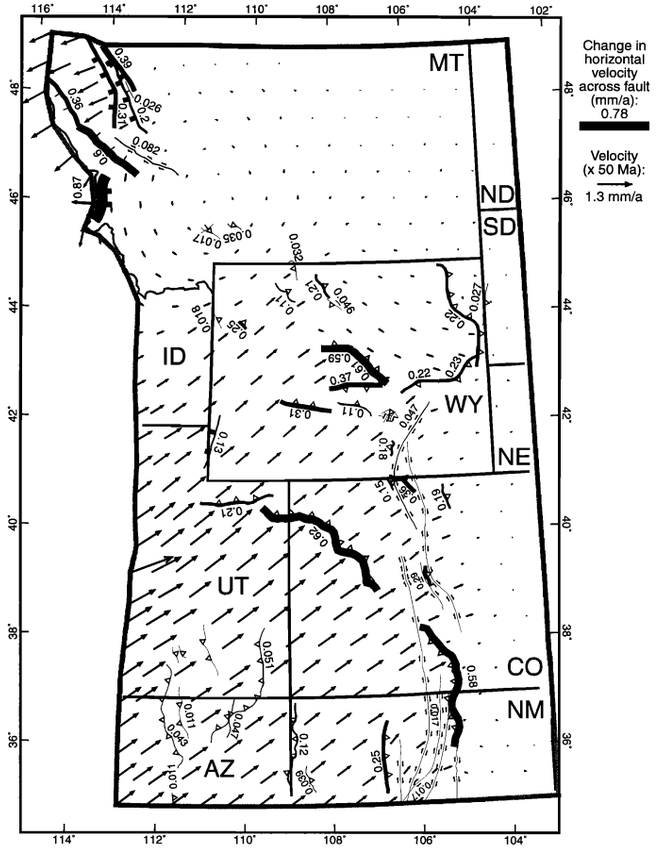

Figure 6. Paleotectonics during 45-40 Ma (middle Eocene). Conventions are as in Figure 3. The Sevier orogeny is over. Foreland velocities are only half as large as in Figure 5, and velocity vectors have rotated clockwise about 15°. The late Laramide structures are generally those farthest to the east and south. Note the beginning of extension in northwest Montana.

Bird, Tectonics, 1998

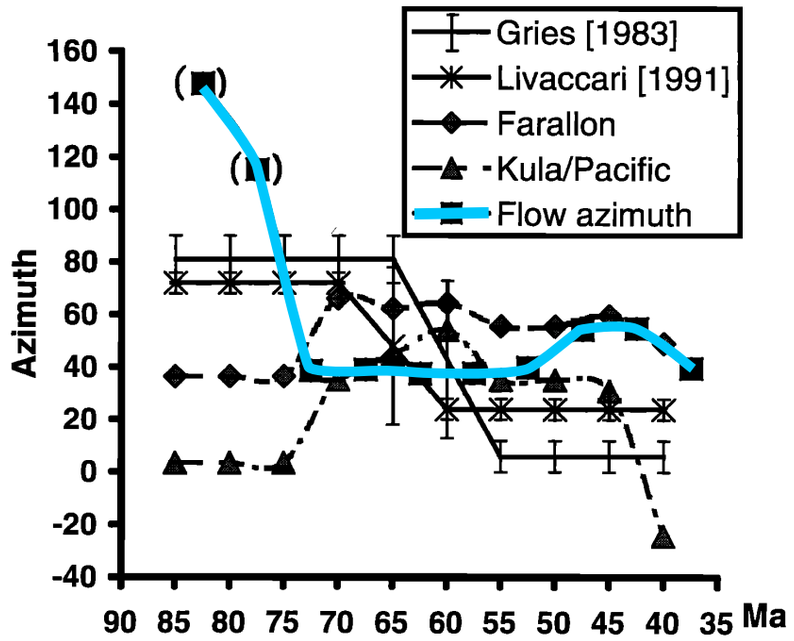

Figure 7. Computed history of the mean azimuth of crustal flow in the Rocky Mountain Foreland and Colorado Plateau (squares), compared to the azimuth histories expected for possible causes. (Crustal flow azimuths are in parentheses until 75 Ma because velocities are very low and these azimuths are probably not reliable.) Curves labeled "Farallon" and "Kula/Pacific" are the azimuths of the velocities of those plates with respect to stable North America at (38°N, 109°W) according to stage poles from *Engebretson et al.* [1985]. Curve labeled "*Gries* [1983]" shows the inferred history of shortening direction that she attributed to changes in the direction of the absolute velocity of North America. Curve labeled "*Livaccari* [1991]" shows the inferred history of shortening direction that he attributed to the rise and fall of segments of the western cordillera. No model is satisfactory for all times. Probably the shortening direction was controlled by slip partitioning and slumping of the cordillera before 75 Ma (early Sevier orogeny) but was then controlled by coupling to one or both subducted oceanic plates during 75-35 Ma (Laramide orogeny). There is a suggestion that azimuth was controlled by the Kula plate before 50 Ma and by the Farallon plate after 50 Ma.

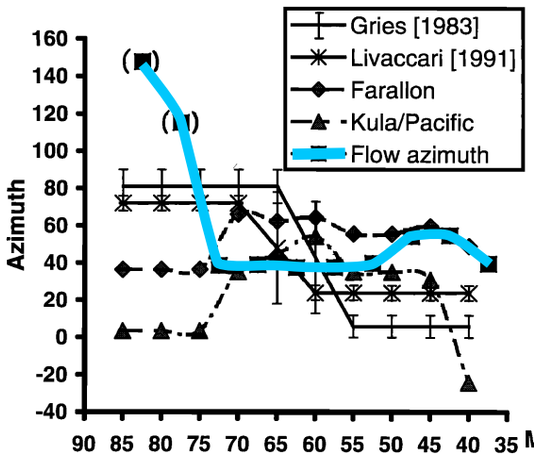

Bird, Tectonics, 1998

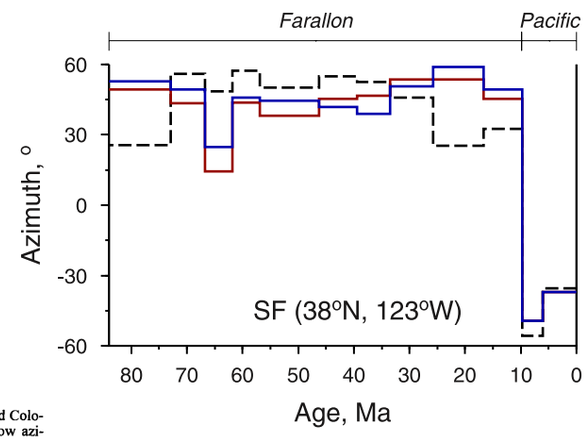

Doubrovine&Tarduno, JGR, 1998

Figure 7. Computed history of the mean azimuth of crustal flow in the Rocky Mountain Foreland and Colorado Plateau (squares), compared to the azimuth histories expected for possible causes. (Crustal flow azimuths are in parentheses until 75 Ma because velocities are very low and these azimuths are probably not reliable.) Curves labeled "Farallon" and "Kula/Pacific" are the azimuths of the velocities of those plates with respect to stable North America at (38°N, 109°W) according to stage poles from *Engebretson et al.* [1985]. Curve labeled "*Gries* [1983]" shows the inferred history of shortening direction that she attributed to changes in the direction of the absolute velocity of North America. Curve labeled "*Livaccari* [1991]" shows the inferred history of shortening direction that he attributed to the rise and fall of segments of the western cordillera. No model is satisfactory for all times. Probably the shortening direction was controlled by slip partitioning and slumping of the cordillera before 75 Ma (early Sevier orogeny) but was then controlled by coupling to one or both subducted oceanic plates during 75-35 Ma (Laramide orogeny). There is a suggestion that azimuth was controlled by the Kula plate before 50 Ma and by the Farallon plate after 50 Ma.

Plate circuit reconstructions tend to increase obliquity of Farallon subduction somewhat (solid lines—blue is Engebretson Far-Pac, red is Mueller Far-Pac, dashed is Engebretson fixed hotspot).